UNDERSTANDING INTERANNUAL VARIABILITY AND TRENDS IN 15 YEARS (1993-2007) OF SATELLITE-DERIVED OCEANIC EVAPORATION

By

Frank J. Kelly

December, 2011

A Thesis Paper Submitted
In Partial Fulfillment of the
Requirements for the Degree of

MASTER OF SCIENCE

Texas A&M University-Corpus Christi
Environmental Science Program
Corpus Christi, Texas

Approved: _____ Date: _____
Dr. A. M. Mestas-Nuñez, Chairperson

_____
Dr. P. Tissot, Member

_____
Dr. J. Smith-Engle, Member

_____
Dean
College of Science and Engineering

ABSTRACT

Warming trends in sea surface temperature during the latter portion of the 20th century have raised inquiries about associated trends in oceanic evaporation. Theory dictates that evaporation increases according to the Clausius-Clapeyron relation. In this study, a 15-yr (1993-2007) dataset based on satellite observations by the French Research Institute for Exploitation of the Sea (IFREMER) is used to estimate interannual variability and trends in latent heat flux (LHF) and associated bulk variables. Comparisons with three satellite datasets, two reanalyses, and a hybrid of the two present both similarities and differences. Interannual variability of evaporation shows spatial structure that is mainly related to El Niño-Southern Oscillation (ENSO) and cold air outbreaks over boundary currents. LHF variability is largely controlled by variability in air-sea humidity difference. Globally-averaged trends in LHF are positive for all seven products, but satellite datasets show an increase in evaporation that is larger and more global in scope. The observed trends in LHF, in which IFREMER is second largest, are mostly attributable to trends in air-sea humidity difference.

Because none of the datasets can be regarded as a "truth," this study helps give an uncertainty range in trend estimates. Discrepancies among datasets arise because of source and derivation of the meteorological variables used in the evaporation algorithm. In particular, IFREMER uses the two-satellite product from *Reynolds et al.* (2007) for sea surface temperature, which creates a ~2 W/m^2 bias high in LHF starting June 2002. Biases in the Special Sensor Microwave Imager (SSM/I) contribute a larger than expected jump in IFREMER's merged wind speed, and thus LHF, around 2002. In addition, IFREMER's humidity algorithm produces a large negative trend in air specific humidity, which enhances the positive evaporation trend.

Table of Contents

List of Figures

List of Tables

Acknowledgements

I would like to thank Dr. Alberto Mestas-Nuñez, Chairman of my committee, for his collaboration and patience during the completion of this thesis, and his support and help given to me throughout my studies at Texas A&M University-Corpus Christi. I would also like to thank Dr. Philippe Tissot and Dr. Jennifer Smith-Engle, members of my committee, for their advice and cooperation in this research.

I am grateful to Dr. Abderrahim Bentamy for providing me with the IFREMER flux product and guiding me on how to thoroughly investigate the dataset. I am also grateful to the remaining members of COMPASS that welcomed me into the air-sea flux community and provided guidance during this research.

The support of the National Science Foundation under grant ATM0631677 to Texas A&M University-Corpus Christi is gratefully acknowledged.

1. INTRODUCTION

Surface evaporation plays a dual role in the global climate system because it participates in worldwide distribution of water and heat. Since the oceans cover more than two-thirds of the Earth's surface, most of the surface evaporation (~86%) occurs over the oceans [e.g. *Baumgartner and Reichel*, 1975]. Evaporation is a difficult quantity to measure regardless of whether it is over land or water because researchers must sample turbulent fluctuations of relevant variables over a wide range of temporal and spatial scales. In addition, the vastness of the ocean makes direct measurements of these variables difficult. Only during the satellite era (late 1970s and beyond) have scientists been able to monitor global surface oceanic and meteorological variables with sufficient spatial coverage for climatic applications. Satellite remote sensing allows estimating oceanic evaporation from measurements of radiation and surface roughness through empirical algorithms refered to as "bulk formulas."

This study reviews the methodology for estimating oceanic evaporation from satellite observations and provides an overview of some previous studies that measure oceanic evaporation, its variability, and trends. The main goal is to analyze evaporation estimates produced by the French Research Institute for Exploitation of the Sea (IFREMER) [*Bentamy et al.*, 2003]. An in depth analysis of interannual variability and trends in the IFREMER evaporation and associated bulk variables is performed, and the results are compared to other flux products to try to understand the reasons for the differences. The results of this work should help determine an uncertainty range in satellite evaporation estimates.

This thesis is organized as follows: In section 2 a review of the bulk flux calculation and background references are provided. The datasets used in this study are described in section 3. The comparison methodology including the calculation of interannual variability and trends is provided in section 4. The results of the comparisons between the various flux products are presented in section 5. Finally, a discussion of the implication of the results and a summary are given in section 6.

2. BACKGROUND

Oceanic evaporation is a determining factor in the global distribution of heat and precipitation. Its influence is felt as part of the larger hydrologic or water cycle. The hydrologic cycle describes the continuous movement of vast quantities of water through the earth's climate system under the direct or indirect influence of solar radiation. The cycle directly affects the climate and the sustainability of life. It is through precipitation that the public perceives the importance of the water cycle. Yet precipitation is only one part of the cycle. Evaporation is just as important because rain does not occur without evaporation. Furthermore, oceanic evaporation serves as an important air-sea interaction that couples the atmosphere to the ocean. The phase change from liquid to vapor prompted by evaporation occurs through a turbulent flux of moisture that transfers both mass and latent heat to the atmosphere. Latent heat flux (LHF) is synonymous with evaporation, but specifically, it represents the measured amount of heat transferred to the atmosphere during evaporation.

The air-sea flux of moisture plays a crucial role in a wide variety of atmospheric and oceanic processes including sea surface temperature (SST) variability [*Zhang and McPhaden*, 2000; *Yu et al.*, 2006; *Grodsky et al.*, 2009], water cycle variability [*Schlosser and Houser*, 2007; *Wentz et al.*, 2007], El Niño variability [*Liu*, 1988; *Lau and Nath*, 1996; *Klein et al.*, 1999; *Mestas-Nuñez et al.*, 2006], and global energy [*Kiehl and Trenberth*, 1997; *Trenberth et al.*, 2009]. The role of LHF is particularly important in the global, surface energy budget. LHF balances incoming solar radiation when combined with longwave radiation (blackbody radiation) and sensible heat flux (flux due to vertical temperature gradient in the air). Of these four main terms, LHF represents the second largest component of the surface heat budget after shortwave radiation [*Kiehl and Trenberth*, 1997]. Moreover, knowledge of latent heat flux combined with the other turbulent fluxes, sensible heat and momentum (or wind stress), can provide a forcing function for ocean models [*Grima et al.*, 1999; *Blanke et al.*, 2002; *Ayina et al.*, 2006].

2.1. Bulk Flux Algorithms

The direct formulation of LHF is based on estimating the covariance of specific humidity and vertical velocity as follows

$$LHF = \rho L_v \overline{w'q'} \tag{1}$$

where ρ is the density of air, L_v is the latent heat of vaporization, q' and w' are the turbulent perturbations of specific humidity and vertical wind velocity, respectively. The overbar denotes a time averaged quantity and the prime refers to fluctuations about the temporal mean of that quantity.

Two common methods for direct measurement of LHF in the open ocean are eddy correlation and inertial dissipation. Eddy correlation calculates LHF by estimating turbulent fluctuations of the vertical wind and mixing ratio [*Fairall et al.*, 1996a]. Inertial dissipation measures the power spectrum of turbulent eddies in the inertial subrange; fluxes are inferred from the energy dissipation in this frequency spectrum [*Large and Pond*, 1982]. The necessary instruments involved in these two methods are expensive and only deployed on research cruises. Additionally, most ships or buoys don't measure vertical velocity, much less turbulent perturbations of vertical velocity. Thus, empirical bulk algorithms represent the most efficient means of estimating evaporation over large portions of the ocean.

Bulk algorithms are empirically derived formulas that parameterize LHF using common meteorological variables. These bulk algorithms make use of Monin-Obukhov Similarity Theory (MOST) [*Monin and Obukhov*, 1954]. MOST postulates that a layer exists near the surface where fluxes are constant; vertical gradients of wind and humidity are determined by height above the surface and by the components that drive turbulence, i.e shear and buoyancy. From MOST, the turbulent flux of latent heat and associated scaling parameters are defined as

$$LHF = -\rho L_v u_* q_* \tag{2}$$

$$u_* = \left[\left(\overline{w'u'}\right)^2 + \left(\overline{w'v'}\right)^2\right]^{1/4} = \left(\frac{\tau}{\rho}\right)^{1/2} \tag{3}$$

$$q_* = -\frac{\overline{w'q'}}{u_*} \tag{4}$$

where u_* and q_* are scaling parameters for friction velocity (or wind) and humidity, respectively. The flux is related to meteorological measurements through a turbulent exchange coefficient,

$$C_E = -\frac{u_* q_*}{U(q_s - q_a)} \tag{5}$$

where q_a is air specific humidity at a specific height above the surface (typically 10 m), and q_s is the interfacial value of specific humidity, or simply the saturation specific humidity. Saturation humidity is computed from the saturation mixing ratio of pure water at a given SST. Many bulk algorithms consider the effects of salinity on saturation humidity by reducing the value by 2%. C_E is the bulk transfer coefficient for water vapor, which is also called the Dalton number. Thus, the bulk parameterization of latent heat flux is given as

$$LHF = \rho L_v C_E U_a (q_s - q_a) \tag{6}$$

where U_a is scalar wind speed at a specified height above the surface (typically 10 m). The two aforementioned, direct measurement techniques serve as ground truth for validating bulk LHF.

According to equation (6) three key properties control the rate of evaporation: heat, humidity, and air movement. The theoretical limit governing the rate of evaporation is given by the Clausius-Clapeyron relation, which defines an exponential relationship between saturation vapor-pressure and temperature. In other words, water vapor content increases exponentially with increasing temperature until saturation humidity is reached. At saturation, the rate of evaporation equals the rate of condensation. Winds aid the

evaporative process by removing water vapor above the surface. The mixing ratio is lowered below the saturation point and further evaporation can occur. This is a simplification of the evaporation process because turbulence plays a major role, but the simplification illustrates the importance of all properties in determining the rate of evaporation. Ultimately, LHF can be estimated from measurements of SST, q_a, and U_a.

Of course, ships and buoys can provide the state variables needed for calculating the bulk flux, but satellite estimates are periodic and truly global in scope. Space-borne instruments can advance the global estimates of evaporation. Many empirical models and satellite instruments are available for estimating these variables, and some of the more common approaches are briefly addressed.

2.2. Satellite Estimates of Bulk Variables

2.2.1. SST

The NOAA products are probably the most widely used for SST, and they include two high resolution SST datasets that use optimum interpolation to combine satellite measurements with *in situ* data [*Reynolds et al.*, 2007]. These datasets have a spatial resolution of 0.25º and a temporal resolution of one day. One utilizes the Advanced Very High Resolution Radiometer (AVHRR), while the other fuses the AVHRR with the Advanced Microwave Scanning Radiometer (AMSR). The first AVHRR was launched in 1979, so it provides a record of global SST for the last 30+ years. The AMSR is still a relatively new instrument (launched in June 2002), so its record length is limited. Unlike the AVHRR, the AMSR has near all-weather coverage because it can "see" through clouds. *Reynolds et al.* [2007] note a variance jump in the analysis with the addition of

the AMSR, which requires fusion of the two disparate instruments. Both products provide useful SST estimates, but some institutions choose the AVHRR-only product over the AVHRR-AMSR product for consistency over the entire 30-yr record.

2.2.2. Wind Speed, U_a

Satellite measured wind speed is often derived from scatterometers or the Special Sensor Microwave/Imager (SSM/I). Scatterometers, such as SeaWINDS onboard the QuickSCAT satellite or scatterometers onboard the European Remote Sensing satellites (ERS-1 and ERS-2), offer many advantages over the SSM/I for measuring ocean winds. A scatterometer is an active microwave radar that sends high frequency radio waves toward the ocean surface and measures the received backscatter. The magnitude of the backscatter is proportional to the surface roughness, which is a measure of wind stress. In addition, the power of the backscatter is a function of wind speed and direction; therefore, a scatterometer provides measurements of vector winds.

Conversely, the SSM/I, which is carried aboard satellites from the Defense Meteorological Satellite Program (DMSP), is a passive radiometer that measures microwave brightness temperatures (T_B) at four separate frequencies: 19.35, 22.235, 37, and 85.5 GHz [*Wentz*, 1997]. The radiation observed by the SSM/I antennae is a mixture of radiation emitted by the sea surface and the atmosphere. Sea surface characteristics affecting the emitted radiation include sea surface temperature and surface roughness, while atmospheric characteristics include atmospheric temperature and moisture content, i.e. water vapor and clouds [*Wentz*, 1997]. Empirical models relate the brightness temperatures at given frequencies to wind speed; still other frequencies are used to

correlate T_B with water vapor or liquid water. A drawback to the empirical models is they generally estimate surface wind speed better than vector winds [*Wentz and Ashcroft*, 1996]. This drawback does not inhibit calculations of LHF since only wind magnitude is necessary, but wind vectors are required when forcing ocean models.

2.2.3. Near-surface Specific Air Humidity, q_a

The SSM/I is the most commonly used instrument for estimating near-surface humidity. Of the three properties required to estimate evaporation, humidity is the most difficult to measure from space. As a result, many empirical algorithms have been proposed and refined to measure near-surface humidity using SSM/I brightness temperatures [e.g., *Liu*, 1986; *Schulz et al.*, 1993; *Schlussel et al.*, 1995; *Schulz et al.*, 1997; *Bentamy et al.*, 2003].

The SSM/I estimates total column water vapor relatively well, but the main difficulty comes from estimating humidity at a given height, e.g. 10 m. Initial research tried to relate total column water vapor with q_a [*Liu*, 1986] but the results showed systematic biases over large regions of the globe [*Bentamy et al.*, 2003]. It has been shown that empirical models with the lowest bias are directly derived from SSM/I brightness temperatures [*Schulz et al.*, 1997; *Bentamy et al.*, 2003]. These models use multivariate linear regression to correlate certain frequency channels of the SSM/I with q_a. Even with improvements to q_a over the years, though, humidity remains the largest source of error when estimating LHF [*Bourras*, 2006; *Iwasaki*, 2010].

2.2.4. Moisture Transfer Coefficient, C_E

In addition to the three key meteorological properties, equation (6) implies knowledge of the transfer coefficient, C_E. Much research has been devoted to developing an accurate bulk algorithm; so many different options are available [e.g., *Liu, Katsaros, and Businger*, 1979; *Smith*, 1988; *Fairall et al.*, 2003; *Chou et al.*, 2003]. Currently the COARE 3.0 flux algorithm [*Fairall et al.*, 2003] is considered the "least problematic" [*Brunke et al.*, 2003]. COARE 3.0 does not use prescribed transfer coefficients; instead, it uses an iterative approach to estimate the stability-dependent, MOST scaling parameters, and fluxes of heat and momentum.

Included within the COARE 3.0 algorithm are sub-models that account for the cool-skin effect of SST at the interface and the influence of wave effects at moderate wind speeds. A cool-skin layer forms in the upper few millimeters of the ocean because of heat lost due to turbulent fluxes and radiation; this layer is 0.1 to 0.5 C cooler than the water immediately below it [*Fairall et al.*, 1996b]. In theory, it is appropriate to use the cool-skin temperature when calculating LHF. In reality, most SST measurements are bulk temperatures, meaning they are taken slightly below the molecular surface layer. The cool-skin model accounts for the slight discrepancy between bulk temperature and skin temperature. At moderate to high wind speeds, the assumption of an aerodynamically smooth surface is no longer valid. The surface roughness alters the effects of turbulence, which in turn, alters the rate of evaporation. Yet, a bulk algorithm does not measure turbulence directly, so sub-models are provided to account for the

effects of waves. The COARE 3.0 algorithm is currently the most complex and state of the art turbulent flux algorithm publicly available.

COARE 3.0 shows the lowest bias when compared with eddy correlation flux measurements, and it is effective over a wide wind domain. Other algorithms are effective at low or even moderate wind speed regimes, but they are inaccurate in high winds. Most importantly, the COARE 3.0 algorithm is suitable for use with daily-averaged variables measured by satellites.

2.3. Previous Satellite Comparison Studies

The SEAFLUX project was created to coordinate research efforts on bulk turbulent fluxes and thus contribute to the improvement of all bulk formulas [*Curry et al.*, 2004]. The main goal of the project is to reduce uncertainty in all areas related to bulk flux estimates and increase the reliability of satellite-based fluxes. In addition, SEAFLUX provides access to most satellite-based flux products which is useful for inter comparisons.

Previous studies have compared satellite LHF products with each other and with reanalyses and *in situ* data [e.g., *Kubota et al.*, 2003; *Chou et al.*, 2004; *Bourras*, 2006]. The most common reanalyses included in comparison studies originate at the major modeling centers such as the National Centers for Environmental Prediction (NCEP) and the European Centre for Medium-Range Weather Forecasts (ECMWF). The reanalysis products incorporate a frozen, numerical weather prediction (NWP) model and a data assimilation system. Reanalyses accomplish this assimilation by constraining a forecast model, which is consistent over the entire analysis period, with observations from the

global meteorological network and some satellites. Reanalyses may represent a baseline for satellite comparisons.

A more straightforward baseline stems from oceanic *in situ* data obtained from buoys and ships of opportunity. For example, the International Comprehensive Ocean-Atmosphere Data Set (ICOADS) [*Worley et al.*, 2005] is an archive of maritime measurements that extends back over 300 years, and it represents a standard of comparison for all calculated turbulent flux datasets. It is important to note that satellite products involved in past inter-comparisons studies were early iterations; improvements have been made to the products since their publication. Nonetheless, investigating older datasets provides insight into the current state of satellite-derived latent heat fluxes.

Kubota et al. [2003] and *Chou et al.* [2004] performed comparison studies of LHF using a combination of satellite, *in situ*, and reanalysis products over a 2-yr and 1-yr period, respectively. *Kubota et al.* [2003] looked at six separate datasets: the Japanese Ocean Flux Data Sets with use of Remote Sensing Observations (J-OFURO) [*Kubota et al.*, 2002], the Hamburg Ocean-Atmosphere Parameters and Fluxes from Satellite Data (HOAPS) [*Grassl et al.*, 2000], the Goddard Satellite-Based Surface Turbulent Fluxes (GSSTF) [*Chou et al.*, 1997], the ECMWF reanalysis, the NCEP-National Center for Atmospheric Research (NCAR) reanalysis (NCEP-R1) [*Kalnay et al.*, 1996], and *da Silva et al.* [1994], which derives from an earlier version of ICOADS.

Chou et al. [2004] used some overlapping datasets including the HOAPS, NCEP-R1, and da Silva products, but they used version 2 of the GSSTF (GSSTF2) [*Chou et al.*, 2003]. The short time frames limited their investigation to mean-annual LHF, and the

influence of wind speed and humidity on LHF. They found that fluxes based solely on *in situ* data may be limited to the Northern Hemisphere due to the lack of observations in the Southern Hemisphere. In addition, the LHF accuracy of global reanalyses depends on the density of assimilated data. Most satellite products tend to overestimate LHF in the tropics and the Southern Hemisphere when compared to reanalyses. A possible cause is smaller estimates of near-surface humidity by the satellites. Furthermore, reanalysis estimates of evaporation in the Southern Hemisphere are often interpolations of available data, so smaller values are not surprising. HOAPS is the only satellite product that gives lower LHF values than reanalyses in the tropics, which likely results from their wind speed estimates.

Bourras [2006] also performed comparisons of LHF using data from five different satellite-based datasets: version 2 of HOAPS (HOAPS2) [*Fenning et al.*, 2006], J-OFURO, GSSTF2, the *Jones et al.* [1999] dataset, and the Bourras-Eymard-Liu (BEL) dataset [*Bourras et al.*, 2002]. He compared these fields with buoy data from the tropics and mid-latitudes. His results show that all satellite products exhibit different magnitudes of rms error and/or bias for different parts of the ocean. In other words, moderate to strong variations in LHF existed when a single satellite product was compared to *in situ* data. All products except the Jones dataset had moderate root mean square (rms) errors and biases in the mid-latitudes. The Jones dataset experienced the largest systematic differences in the tropical Pacific. Overall, he suggests that HOAPS2 is the most adequate satellite product for investigating fluxes over the global oceans.

Bourras [2006] suggests that satellite products are already competitive with *in situ* flux climatologies or reanalyses, despite their errors and obvious differences. His sentiments are likely prompted by the battle between sampling error versus measurement error. Even though the ICOADS dataset is accepted climatology, it may be no better than satellite-derived fluxes because of the lack of observations in the Southern Hemisphere.

2.4. Previous Studies on LHF Variability and Trends

The above studies of satellite latent heat flux were based on datasets that spanned only a few years, so their goals were limited to investigating annual means and associated spatial patterns. Recent satellite-based datasets of evaporation now extend back to the late 1980's or early 1990's since this time frame coincides with the availability of SSM/I and/or scatterometers. Hence, 20 to 30 years of satellite fluxes are now available for studying interannual variability and possibly trends. This record length is too short to rule out a confounding influence from decadal and multi-decadal oscillations; yet, a trend analysis can help in analyzing tendencies in the recent climate and in evaluating the quality of satellite fluxes. Recent warming trends in SST [*Casey and Cornillon*, 2001; *Deser et al.*, 2010] suggest increased oceanic evaporation, and satellite estimates of LHF should contribute to this discussion. These issues have been discussed in past studies and three of the more relevant studies are briefly discussed here.

Schlosser and Houser [2007] assessed the global water cycle, both land and ocean, by using several datasets of evaporation and precipitation. Oceanic evaporation data came from HOAPS and GSSTF2, while land-based evaporation came from the Center for Ocean-Land-Atmosphere Studies (COLA) Global Offline Land surface

Dataset (GOLD). They supplemented the water cycle analysis by using precipitation data from version 2 of the Global Precipitation Climatology Project (GPCP) and the Climate Prediction Center (CPC) Merged Analysis of Precipitation (CMAP). All of these products are derived from satellites except the GOLD product, which is derived from a land surface scheme and an atmospheric model. Their results show that interannual variations in total global evaporation loosely correlate with interannual variations in total global precipitation. However, the estimates of evaporation and precipitation provide a better balance when looking at annual means. One of their most notable findings is a trend in global evaporation which they attributed to the trend in oceanic evaporation as calculated by the HOAPS and GSSTF2 products. A complementary trend in precipitation is not seen. The most apparent cause for the LHF trend is transitions between SSM/I instruments, which causes jumps in q_a and U, and thus, in LHF as well. In the end, they conclude that satellite measurements cannot yet satisfactorily describe water cycle variability.

Yu and Weller [2007] examined trends and interannual variations of surface turbulent heat flux, i.e., latent and sensible heat flux, using the Woods Hole Oceanographic Institution's (WHOI) objectively analyzed air-sea fluxes (OAFlux) [*Yu et al.*, 2008]. They show that the equatorial Pacific and Indian oceans, as well as the Western Boundary currents, exhibit the largest interannual variability. In all areas except the Indian Ocean, LHF variability is highly correlated with SST variability. Global trends over the ice-free oceans from 1981 to 2005 are identified in LHF and SST. Trends in SST are marked by large interannual variations associated with ENSO. The LHF trend

does not exhibit these variations, yet the results suggest that the LHF trend is a response to the SST trend. The variable that links the two trends is the humidity difference, q_s - q_a or Δq. A trend is also seen in wind speed, but its role is to boost the effect of Δq.

Liu and Curry [2006] also examined trends and interannual variability of LHF using four datasets: GSSTF2, HOAPS2, the 40 year reanalysis produced by the ECMWF (ERA-40) [*Uppala et al.*, 2005], and the NCEP-Department of Energy (DOE) reanalysis (NCEP-R2) [*Kanamitsu et al.*, 2002]. They confirm a trend in evaporation as well from 1989 to 2000, but their analysis is restricted to the tropical and sub-tropical oceans (35ºS–35ºN). The magnitude of the positive trend was significant at the 95% confidence level in all but one of the datasets (ERA-40), but it varies considerably between datasets. Unlike the other studies, Liu and Curry performed statistical significance tests on all calculated trends. They attribute the positive trend in LHF to a significant positive trend in wind speed. They also determined that the positive trend in evaporation is independent of ENSO.

3. DATASETS

Seven monthly latent heat flux products from satellites, reanalyses, or a combination of the two are compared in this study. Table 1 lists the properties and references of the seven datasets and suggests that differences in the determination of LHF may arise from the different sources of the three main input state variables as well as the type of bulk flux algorithm used. The products are divided into two broad categories based on their input source: satellite and renalysis/hybrid.

The four satellite products used for this investigation are version 2b of the GSSTF (GSSTF2b) [*Shie et al.*, 2009], version 3 of HOAPS (HOAPS3) [*Andersson et al.*, 2010], the IFREMER fluxes, and version 2 of J-OFURO (J-OFURO2) [*Tomita et al.*, 2010]. Most of these datasets rely solely on input data from satellite measurements; however, the GSSTF2b utilizes SST from the NCEP-R2. *Smith et al.* [2010] classifies the GSSTF2b as a hybrid product, but since it is largely based on satellite data, it is classified as a satellite product here.

The three reanalysis/hybrid products used for this investigation are the interim reanalysis project from ECMWF (ERA-Interim) [*Dee et al.*, 2011], NCEP-R2, and OAFlux. The NCEP products (both R1 and R2) are common reanalyses used for comparison studies. Only NCEP-R2 is included here because it is considered an updated version of the original NCEP reanalysis. The ERA-Interim is also an updated reanalysis because it extends and improves upon the ERA-40. OAFlux is unique because it combines meteorological variables from satellites with those from reanalyses; here it is grouped with the other reanalyses because it incorporates large amounts of info from NCEP-R1, NCEP-R2, and the ERA-40.

Each of the monthly products analyzed in this study are available over vastly different time periods. In addition, many of the products use different horizontal grid resolutions. To facilitate comparisons, each product was temporally trimmed to a common time period, January 1993 – December 2007, and bilinearly interpolated to a 1° × 1° grid resolution if the native resolution was not already partitioned in this manner. HOAPS3 and J-OFURO2 do not extend all the way to 2007, so their temporal extents

terminate in 2005 and 2006, respectively. Variables from NCEP-R2 were downloaded at a 6-h timestep; therefore, the 6-h data were monthly-averaged for consistency with the other products. Also, the native resolution of the ERA-Interim is a TL255 Gaussian grid (nominally 0.75°). Yet, the ECMWF public server only provides data at a 1.5° resolution, so this reduced resolution was used here. A common 1° × 1° land mask was applied to all datasets. The land mask was created by combining land masks from each product, and then taking the largest coincident mask that applied to all grids. Relevant aspects of each product will be discussed in more detail in the subsections that follow.

Table 1. Description and references for the seven flux products used in this study. All the datasets were monthly except NCEP-R2, which was 6-hourly.

	Satellite			
	GSSTF2b	HOAPS3	IFREMER	J-OFURO2
Resolution	1° x 1°	0.5° x 0.5°	1° x 1°	1° x 1°
Period	Jul 1987 – Dec 2008	Jul 1987 – Dec 2005	Mar 1992 – Dec 2007	Jan 1988 – Dec 2006
Wind Speed	SSM/I *Wentz (1997)*	SSM/I Neural Network *Andersson et al. (2010)*	SSM/I, ERS-1, ERS-2, & QSCAT *Bentamy et al. (1999)*	ERS-1/2, QSCAT, AMI, AMSR-E, TMI, & SSM/I *Kubota & Tomita (2007)*
SST	NCEP R2 *Kanamitsu Et al. (2002)*	Pathfinder V5.0 *Casey (2004)*	NOAA OISST V2: AVHRR + AMSR *Reynolds et al. (2007)*	JMA MGDSST *Kurihara et al. (2006)*
Humidity	SSM/I *Chou et al (1995,1997)*	SSM/I *Bentamy et al. (2003)*	SSM/I *Bentamy et al. (2003)*	SSM/I *Schlussel et al. (1995)*
Bulk Formula	*Chou (1993)*	COARE 3.0 *Fairall et al. (2003)*	COARE 3.0 *Fairall et al. (2003)*	COARE 3.0 *Fairall et al. (2003)*

Table 1. (continued).

	Reanalysis/Hybrid		
	ERA-Interim	NCEP-R2	OAFlux
Resolution	TL255, (Nom. 0.75°)	T62, (Nom. 1.875°)	1° x 1°
Period	Jan 1989 – Pres.	Jan 1979 – Pres.	Jan 1958 – Pres.
Wind Speed	*Dee et al. (2011)*	*Kanamitsu et al. (2002)*	QuickSCAT, SSM/I, AMSR-E, NCEP R1/R2, & ERA-40 *Yu et al. (2008)*
SST	*Dee et al. (2011)*	*Kanamitsu et al. (2002)*	NOAA OISST V2: AVHRR only, NCEP R1/R2, & ERA-40 *Yu et al. (2008)*
Humidity	*Dee et al. (2011)*	*Kanamitsu et al. (2002)*	SSM/I *Chou et al. (1995,1997)*
Bulk Formula	*Beljaars (1995)*	*Kanamitsu et al. (2002)*	COARE 3.0 *Fairall et al. (2003)*

3.1. Satellite Products

The GSSTF2b is an extended and slightly improved version of the GSSTF2, which was only produced for a 13-yr period (July 1987 – December 2000). Improvements include use of the SSM/I V-6 product from Remote Sensing Systems (RSS) for determining T_B, precipitable water, and wind speed. Also, SST comes from NCEP-R2 instead of NCEP-R1. GSSTF2b still employs an EOF method for calculating q_a using SSM/I measurements of total precipitable water (W) and bottom-layer precipitable water (W_B) [*Chou et al.*, 1995, 1997]. The bulk algorithm used in the GSSTF2b remains the same as well; it is based on the algorithm from *Chou et al.* [1993]. Two separate sets of the GSSTF2b are available: Set1 and Set2. Set1 contains a larger, global temporal trend in latent heat flux, so Set2 was created using less data from satellites that appeared to have a large trend [*Shie*, 2010]. The trade off is less/more

missing data from Set1/Set2. Yet, the selection process for Set2 was subjective, so Set1 was used here because it included all available data.

The HOAPS3 is a satellite dataset comprised of all available SSM/I data from the various DMSP missions (i.e. F08, F10, F11, F13, F14, and F15). HOAPS3 tries to preserve long term homogeneity in all its variable estimates by only using the SSM/I except for SST, where it uses the AVHRR. In addition, it does not use NWP data, so it stands as an independent, satellite dataset of LHF. Wind speed is directly derived from brightness temperatures using a neural network adapted from *Krasnopolsky et al.* [1995]. Specific humidity is calculated using the regression coefficients from *Bentamy et al.* [2003], which are correlated with the 19, 22, and 37 GHz channels of the SSM/I. SST is taken from the NOAA National Oceanographic Data Center (NODC) and Miami Rosenstiel School of Marine and Atmospheric Science (RSMAS) Oceans Pathfinder Version 5.0 [*Casey*, 2004]. Saturation specific humidity is calculated from SST using the Magnus formula [*Murray*, 1967] with a correction factor of 0.98 to account for salinity effects. HOAPS3 (and remaining satellite datasets) implements the COARE 3.0 bulk flux algorithm to calculate latent heat, but it does not implement the sub-models.

IFREMER is a multi-satellite, multi-instrument dataset that relies on measurements from scatterometers and microwave radiometers. Wind speeds are primarily derived from scatterometers aboard the ERS-1, ERS-2, and the QuickSCAT; however, SSM/I wind speeds enhance the wind product when scatterometer retrievals are unavailable. The wind algorithm comes from *Bentamy et al.* [1999]. IFREMER utilizes the dual instrument version of Reynolds SST analysis [*Reynolds et al.*, 2007], which

merges the AMSR with the AVHRR beginning June 2002. The same empirical q_a algorithm and COARE 3.0 algorithm used HOAPS3 are implemented in IFREMER.

J-OFURO2 also uses a variety of instruments from different satellites. Wind speed is constructed from measurements taken by all SSM/I's, the AMSR-E, the Tropical Rainfall Measuring Misson (TRMM) Microwave Imager (TMI), the active microwave instrument (AMI), and the same scatterometers in IFREMER. Humidity is based on the *Schlussel et al.* [1995] formula, which is similar to the *Bentamy et al.* [2003] formula but with different coefficients. The F15 satellite is excluded from the humidity analysis. J-OFURO2 uses the Merged Satellite and In situ Data Global Daily SST (MGDSST) from the Japan Meteorological Agency (JMA) to formulate its estimates of saturation humidity. The MGDSST merges *in situ* data with AMSR-E and AVHRR observations. While J-OFURO2 implements the COARE3.0 algorithm, it is unclear whether it implements the cool-skin or wave sub-models.

3.2. Reanalysis/Hybrid Products

ERA-Interim is the latest generation of reanalysis from the ECMWF. It is an updated version of the ERA-40 that addresses certain data assimilation problems and issues related to data selection, quality control, and bias correction. It uses a 12-hourly 4DVar assimilation scheme where an upper-air variational analysis is followed by a, separate near-surface analysis. *Dee et al.* [2011] points out that the 4DVar scheme shows improvements over the 3DVar scheme implemented in the ERA-40. ERA-Interim incorporates the same data as the ERA-40 with additional information from updated

satellite instruments. The bulk algorithm used in the ERA-Interim comes from *Beljaars* [1995], who based stability functions on *Holtslag and de Bruin* [1988] and *Dyer* [1974].

The NCEP-R2 is a separate reanalysis that tries to fix certain problems that arose after constructing the previous NCEP reanalysis. It assimilates similar observational data as the ECMWF reanalysis while using a slightly older 3DVar technique and 1990's era NWP model.

WHOI's OAFlux is different from all previously mentioned LHF products because it is a fusion of multiple datasets including reanalyses and satellite observations. WHOI uses both NCEP reanalyses and the ERA-40 as input to the objective analysis. Satellite-based winds come from the SSM/I (Wentz algorithm), ASMR-E, and QuickSCAT. For satellite SST, OAFlux utilizes the Reynolds SST analysis that is created only from the AVHRR. Satellite humidity is based on the SSM/I using *Chou et al.* [1995,1997]. Using a variational objective analysis, OAFlux synthesizes NWP and satellite data. It performs this synthesis for each of the relevant bulk variables using an ordinary least squares estimator, which is based on the Gauss-Markov theorem. Furthermore, error covariances that are based on *in situ* data determine the weights or contributions of each inputted product to the final estimates of each bulk variable. For humidity, ERA-40 had some of the largest weights, while satellites had larger contributions to SST and wind [*Santorelli et al.*, 2011]. After the objective analysis, the best estimates of the bulk variables are inputted to the COARE 3.0 algorithm with inclusion of a wave sub-model.

4. METHODS

Interannual variability and trends for the seven different products are examined using monthly estimates of LHF, SST, U_a, and q_a over a large portion of the global, ice-free oceans (45°S – 45°N). As mentioned, SST is used to calculate the saturation specific humidity, q_s. SST differences between satellite and reanalysis products are typically smaller than differences in the other two state variables [*Liu and Curry*, 2006; *Smith et al.* 2011]. The similarity in SST exists because most flux products incorporate the Reynold's SST analysis into their own studies. Therefore, only the humidity difference, Δq, is used for this investigation because differences in Δq largely result from differences in q_a.

4.1. Interannual Variability

Interannual variability is quantified using the standard deviation of climatological means

$$\sigma = \sqrt{\frac{\sum_{n=1}^{N} \left(x_n - \bar{x} \right)^2}{N-1}} \tag{7}$$

where σ is the standard deviation, x_n is the yearly-averaged mean of a given quantity, $\overline{x}$ is the long-term annual mean of a given quantity, and N = 15 yr except for HOAPS3 and J-OFURO2, where N = 13 yr and N = 14 yr, respectively. The calculated standard deviation gives the variation seen in the data on year-to-year or longer time scales.

4.2. Trend Calculation

Since LHF and the associated meteorological variables are environmental time series, it is reasonable to assume that the data are autocorrelated and highly variable.

Both of these attributes make trend detection difficult. Data with positive autocorrelation increase the length of trend-like segments, while data with a high variance tend to obscure deterministic signals. To account for these factors the following model according to *Tiao et al.* [1990] will be used here

$$Y_t = \mu + \omega X_t + S_t + N_t \tag{8}$$

where t = 1,…,T, Y_t is the estimated LHF or one of the state variables, μ is an offset, ω is the magnitude of the linear trend, X_t is the time function represented as a monthly variable, S_t is a seasonal component defined as

$$S_t = \sum_{j=1}^{m} \left\{ A_j \sin\left(\frac{2\pi jt}{12}\right) + B_j \cos\left(\frac{2\pi jt}{12}\right) \right\} \tag{9}$$

where the sines and cosines for a given period *j* represent a different harmonic associated with the seasonal cycle, and up to *m* harmonics are used to fully explain the seasonal cycle. Most environmental time series require four harmonics at most, but the total varies depending on the dataset being investigated. N_t is the unexplained portion of the data, or error term, and it follows an autoregressive (AR) model with order *AR(p),*

$$N_t = \Phi_1 N_{t-1} + \ldots + \Phi_p N_{t-p} + a_t \tag{10}$$

where *p* is the number of correlation parameters, Φ, in the model. Autoregressive models express the current observation as a linear function of previous observations plus a homoscedastic noise term, a_t, which is also referred to as independent white noise. The linear model in (8) is calculated through a generalized least squares fit of the data with a covariance structure of the errors to account for autocorrelation. From the resultant

model, the trend, ω, is determined and significant trends are those exceeding the 95% confidence level.

Determination of m and p is completed through a two-step process. The two-step process is applied to a globally-averaged (45°S – 45°N) time series of LHF or a bulk variable for each product. First, equation (8) is fitted to the data using the first four harmonics ($m = 4$) calculated by (9), but with no autoregressive model for the errors. The partial-autocorrelation of the residuals is plotted, and the maximum, significant lag is chosen as the value of p. Second, equation (8) is re-fitted to the data using (10) and the chosen p as the model for the errors. A similar model with one less harmonic is also fitted to the data. Then, an ANOVA is applied to the two models to determine the significance of the added harmonic. An insignificant model does not require the added harmonic. Successive ANOVAs are conducted until loss of the higher harmonics becomes significant.

Table 2 shows the chosen m and p for each quantity and product. According to Table 2, virtually all products require an AR(3) model to account for the autocorrelation seen in LHF. Thus, LHF typically contains correlation up to three lags. In addition, Table 2 shows that all variables require at least two harmonics to model the seasonal cycle, which means the annual and semi-annual harmonics explain most of the seasonality seen in the various time series.

This two-step process is straightforward when applied to the globally-averaged quantities; however, it becomes time consuming and requires extensive computer resources when applied to the entire gridded products. Hence, it is assumed that the

globally-derived parameters apply everywhere. Trend maps for each product are calculated using the properties listed in Table 2 but with a specified reduction in the order, *p*. All models that have an order greater than one are reduced to an AR(1) model. The reduction in order saves on computer time without significantly affecting the results.

Table 2. The number of harmonics, m, and the order, p, of the auto-regressive model of the errors that fit the data of the seven products for LHF, wind speed (Ua), and humidity difference (Δq).

	GSSTF2b	HOAPS3	IFREMER	J-OFURO2	ERA-Interim	NCEP-R2	OAFlux
				Number of Harmonics, *m*			
LHF	2	3	2	2	2	4	2
U_a	2	3	3	2	2	2	2
Δq	4	2	2	3	3	2	2
				Order of AR model, *p*			
LHF	3	2	3	3	3	3	3
U_a	0	2	2	0	0	0	0
Δq	2	1	1	2	2	2	2

5. RESULTS

To fully understand patterns of interannual variability and trends in evaporation, this study examines spatial and temporal differences. The following will first look at the spatial distribution of interannual variability seen in the seven different products. Differences in variability among the products are summarized using global means. Then, temporal variability is examined using global time series. From these time series, trends are derived and discussed. Finally, the spatial distributions of the trends are explored to understand their origins.

5.1. Spatial Patterns of Interannual Variability

5.1.1. LHF

The standard deviation maps of annually averaged LHF describing the spatial structure of interannual variability in the seven datasets are presented in Figure 1. A similar large-scale, spatial pattern is seen in all the maps but the magnitudes differ considerably. As in *Yu and Weller* [2007], the areas of larger interannual variability occur in the eastern equatorial Pacific and the western boundary currents along the east coasts of North America and Japan. All products except the GSSTF2b experience the greatest amount variation (~ 25 W/m^2) in the western boundary current regions. In the equatorial Pacific, GSSTF2b and HOAPS3 show the largest flux variability (~20 W/m^2). All datasets show relatively higher values of LHF variability off the north-east coast of Australia with IFREMER, GSSTF2b, and particularly NCEP-R2 exhibiting the stronger values (~15-20 W/m^2). IFREMER, GSSTF2b, and NCEP-R2 also show elevated (~12-16 W/m^2) LHF variability in the sub-tropical Indian ocean.

The spatial pattern of LHF for NCEP-R2 is the most different from all the products showing broader areas of high variability. Specifically, the NCEP-R2 variability in the Pacific extends beyond the equatorial region into the Northern and Southern sub-tropical regions. In addition, the NCEP-R2 experiences a second maximum off the west coast of South America in addition to the maximums seen in the boundary currents. Overall, the satellite products tend to show more variability over all the oceans when compared to the reanalysis/hybrid products.

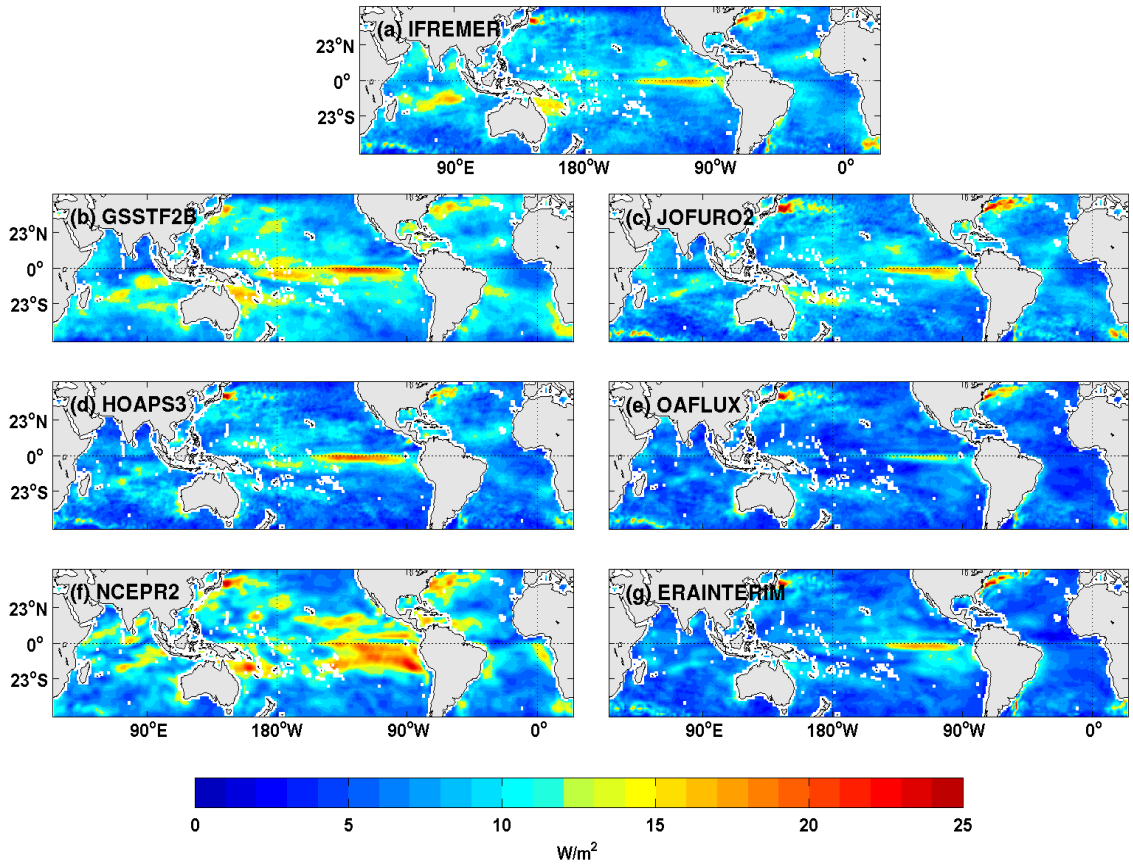

Figure 1. Standard deviation of the yearly-averaged LHF (in W/m2) for (a) IFREMER, (b) GSSTF2b, (c) J-OFURO2, (d) HOAPS3, (e) OAFlux, (f) NCEP-R2, and (g) ERA-Interim. Standard deviation is calculated for the common period January 1993 through December 2007, except for (c) and (d) whose period ends on December 2006 and December 2005, respectively. White areas over ocean regions represent 1° grid cells that are either defined as land or contain missing data.

5.1.2. Wind speed

The interannual variability of wind speed (U_a) seen Figure 2 reveals some clues about the interannual variability of LHF. Most notably, a regional, U_a maximum occurs in the Eastern equatorial Pacific in all products, but this maximum is subdued in the

ERA-Interim. Thus, the equatorial maximums seen in LHF (Figure 1) coincide with the equatorial maximums seen in wind speed.

A second region of increased U_a variation occurs in the central-western, equatorial Pacific in all products. This second region is distinctly different from the region in the eastern Pacific. The magnitude of variation in the second region is weakest in IFREMER and strongest in NCEP-R2. The bi-modal pattern seen in the variability of U_a is likely due to the El Niño-Southern Oscillation (ENSO). In the eastern Pacific, the pattern resembles a canonical ENSO pattern, while the pattern seen in the central Pacific resembles a less traditional and less common Modoki ENSO [*Ashok et al.*, 2007]. Even though the goal of this study is not to investigate ENSO, the fact that all products reveal this pattern is interesting nonetheless.

As noted earlier, the NCEP-R2 exhibits a unique pattern in interannual variability of U_a when compared to the other products. It shows increased U_a variability in most oceans. Variations are quite strong in the high latitudes of the Pacific, the equatorial Indian Ocean, and off the west coast of South America. It is unclear why NCEP-R2 exhibits such a distinctly different pattern.

The magnitude of variability in U_a is quite weak in the boundary current regions for all products. Therefore, wind speed does not account for the LHF variability over the boundary currents. Overall, both satellite and reanalysis/hybrid products show similar magnitudes of interannual variability in wind speed.

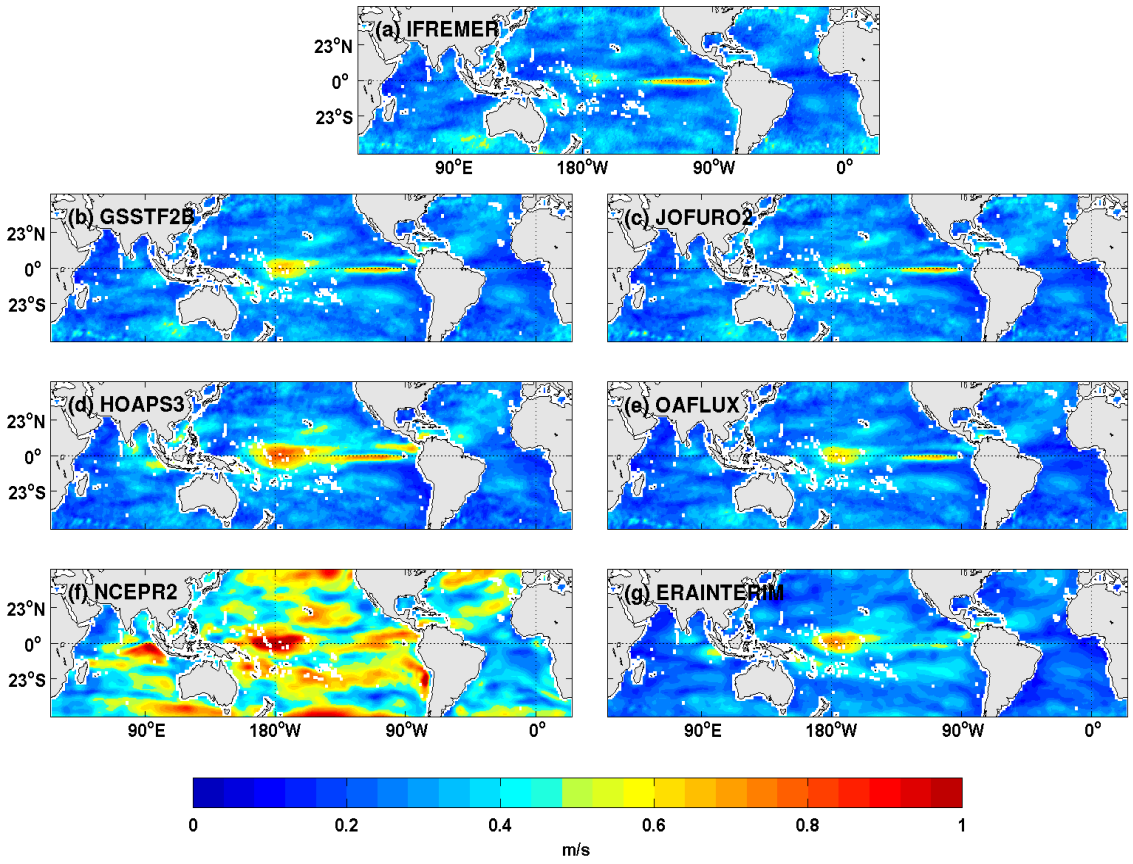

Figure 2. As in Figure 1, except for wind speed, Ua.

5.1.3. Humidity difference

Figure 3 shows the interannual variability of the air-sea humidity difference (Δq) for all seven products. The overall spatial pattern is similar amongst all of the products. In fact, the observed pattern in Δq largely correlates with the pattern seen in LHF. Variability in Δq exhibits some of the largest magnitudes in the equatorial Pacific and cold tongue regions, as well as along the western boundary currents. IFREMER has the lowest magnitudes of Δq variability in the equatorial Pacific compared to ERA-Interim, which has the highest magnitudes.

Variability along the equator resembles interannual variability of SST (not shown), typically associated with ENSO. In turn, saturation specific humidity dominates the pattern of variability seen in Δq. The largest magnitudes of Δq in the reanalysis/hybrid products are shifted to the central-western Pacific, unlike in the satellite products. A possible explanation for the shifted pattern lies in the derivation of Δq. Spatial variability in SST is very similar for most of the products, more so than any other variable. The differences seen in the spatial variability of Δq likely result from differences in spatial variability of near-surface humidity, q_a.

Compared to the other products, ERA-Interim also exhibits an unusual pattern in Δq along the equator. The pattern resembles the Tropical Atmosphere-Ocean (TAO) array of moored buoys. It is plausible that ERA-Interim relies heavily on the TAO array during the assimilation process in this region, which leads to the observed structure seen in Δq. Overall, interannual variability of Δq, as opposed to U_a, appears to have a larger controlling influence over the interannual variability of LHF.

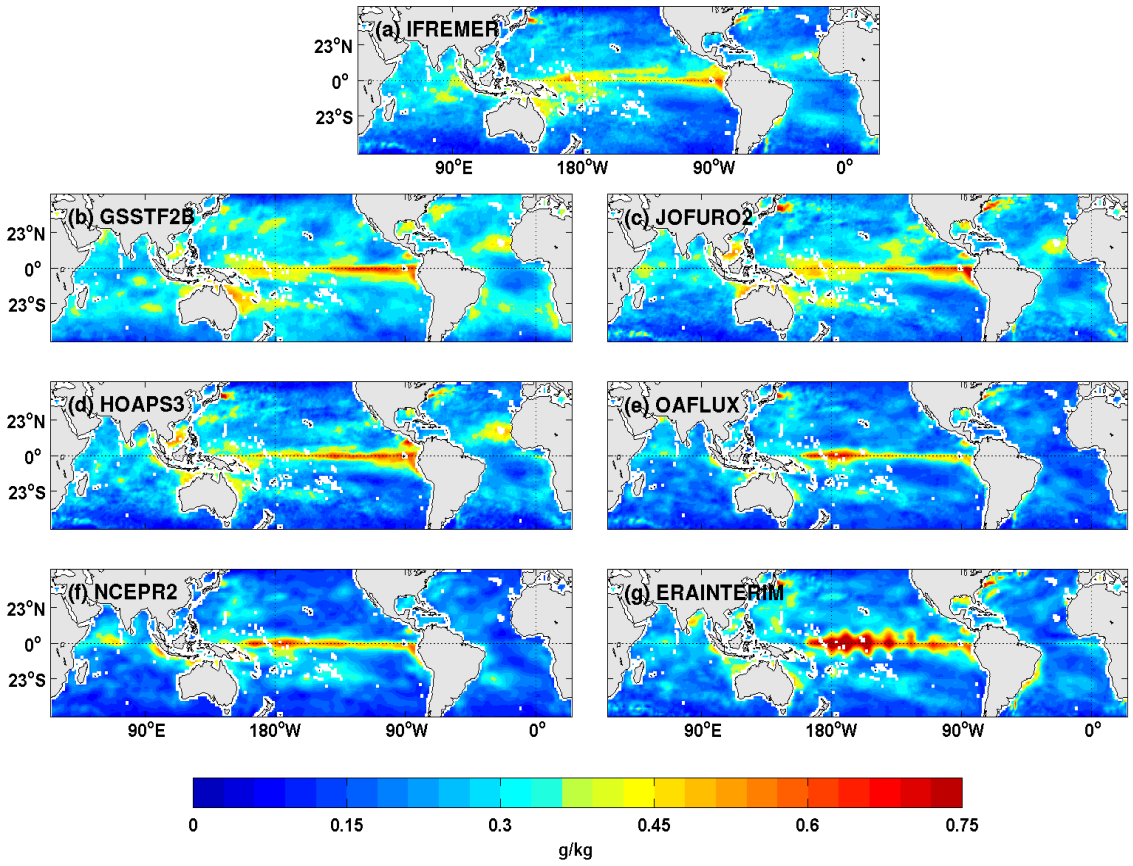

Figure 3. As in Figure 1, except for humidity difference, Δq.

5.1.4. Summary statistics for interannual variability

Table 3 summarizes the interannual variability exposed in Figures 1-3, plus it gives the annual means. From Table 3, it is apparent that NCEP-R2 has the largest annual-mean latent heat flux (134.0 W/m^2) and the largest standard deviation of flux (9.56 W/m^2). GSSTF2b presents a similar magnitude of variability, whereas the other two products in the reanalysis/hybrid category have a much smaller standard deviation (~6.5 W/m^2). IFREMER, HOAPS3 and J-OFURO2 have standard deviations in between these extremes. As a whole, satellite products suggest interannual variability of LHF is

higher than do reanalysis/hybrid products. Annual means of LHF vary too much to classify the two sets of products.

When looking at wind speed in Table 3, all satellite products plus the ERA-Interim and OAFlux have similar annual means (~7 m/s). These same products also show similar magnitudes for the standard deviation of U_a (~0.28 m/s). Only the NCEP-R2 presents a dramatic difference in wind speed; it has the lowest annual mean (5.0 m/s) and the highest standard deviation (0.48 m/s). Thus, all products present a similar global picture for wind speed except the NCEP-R2. This fact was also pointed out in the standard deviation map of U_a (Figure 2).

For the humidity difference in Table 3, annual means range from 3.93 g/kg for NCEP-R2 to 4.73 g/kg for ERA-Interim. The mean values are generally closer to each other amongst the satellite-based datasets. Standard deviations range from 0.209 g/kg for NCEP-R2 to 0.292 g/kg for GSSTF2b. The standard deviations for Δq and LHF do not display the same correspondence apparent in the spatial patterns. Yet, the standard deviations of Δq separate the two sets of products distinctly. Magnitudes of Δq are moderate to high for the satellites and mostly low for the reanalysis/hybrid products.

Table 3. Global, annual mean and interannual standard deviation of LHF, Ua, and Δq for the period January 1993 through December 2007, except for HOAPS3 and J-OFURO2 whose periods end on December 2005 and December 2006, respectively.

	Satellite				Reanalysis/Hybrid		
	GSSTF2b	HOAPS3	IFREMER	J-OFURO2	ERA-Interim	NCEP-R2	OAFlux
LHF (W/m²)							
Annual Mean	118.9	113.3	120.7	110.1	122.2	134.0	110.2
Standard Dev.	9.54	7.57	8.44	8.24	6.76	9.56	6.39
Ua (m/s)							
Annual Mean	7.30	7.50	7.47	7.41	6.84	5.01	7.31
Standard Dev.	0.284	0.296	0.291	0.278	0.277	0.477	0.270
Δq (g/kg)							
Annual Mean	4.55	4.27	4.50	4.26	4.73	3.93	4.19
Standard Dev.	0.292	0.247	0.245	0.270	0.247	0.209	0.218

5.2. Temporal Variability of Globally Averaged Ocean Fluxes

Temporal variability of LHF and its associated state variables are analyzed using time series of the globally-averaged (45°S – 45°N) data. Figures 4-6 present the resultant time series. To generate each time series, the respective seasonal cycle is first removed, and then the variables are low-pass filtered using a 5-month, centered moving average. Filtering reduces much of the noise created by intraseasonal variability, and makes the plots more readable. To supplement the time series plots, Table 4 presents values of the global trend, where significant trends are in bold face.

5.2.1. LHF

Figure 4, which shows the anomaly time series of LHF, separates the products into satellites (top) and reanalysis/hybrid (bottom). All products show similar temporal variations for the first half of the time period. For the second half, all products evolve somewhat similarly, but the magnitudes are greater in the satellites than in the reanalyses

or OAFlux. The 1997-1998 ENSO, which is one of the strongest on record, is evident in all products.

Clearly, the most glaring characteristic-difference between the top and bottom panels of Figure 4 is the trend in LHF. From 1993 to 2007, NCEP-R2, WHOI, and ERA-Interim exhibit a smaller trend in LHF relative to the satellite products; NCEP-R2 shows the highest significant trend (0.49 W/m^2/decade) in comparison to the other two reanalysis/hybrid products (Table 4). Conversely, all of the satellite products exhibit a more pronounced trend in LHF with IFREMER and GSSTF2b being the largest.

The IFREMER trend is dominated by a specific segment of the data, i.e., the rapid increase in LHF centered around 2002. The GSSTF2b trend is also driven by a rapid increase in LHF near 2000; however, the lower anomaly at the beginning of the time period contributes to the overall larger trend. LHF trends for all satellites products are significantly positive with a range of 0.77 to 1.23 W/m^2/decade (Table 4). Looking at the time series of the state variables should reveal more information into the causes of these trends in latent heat.

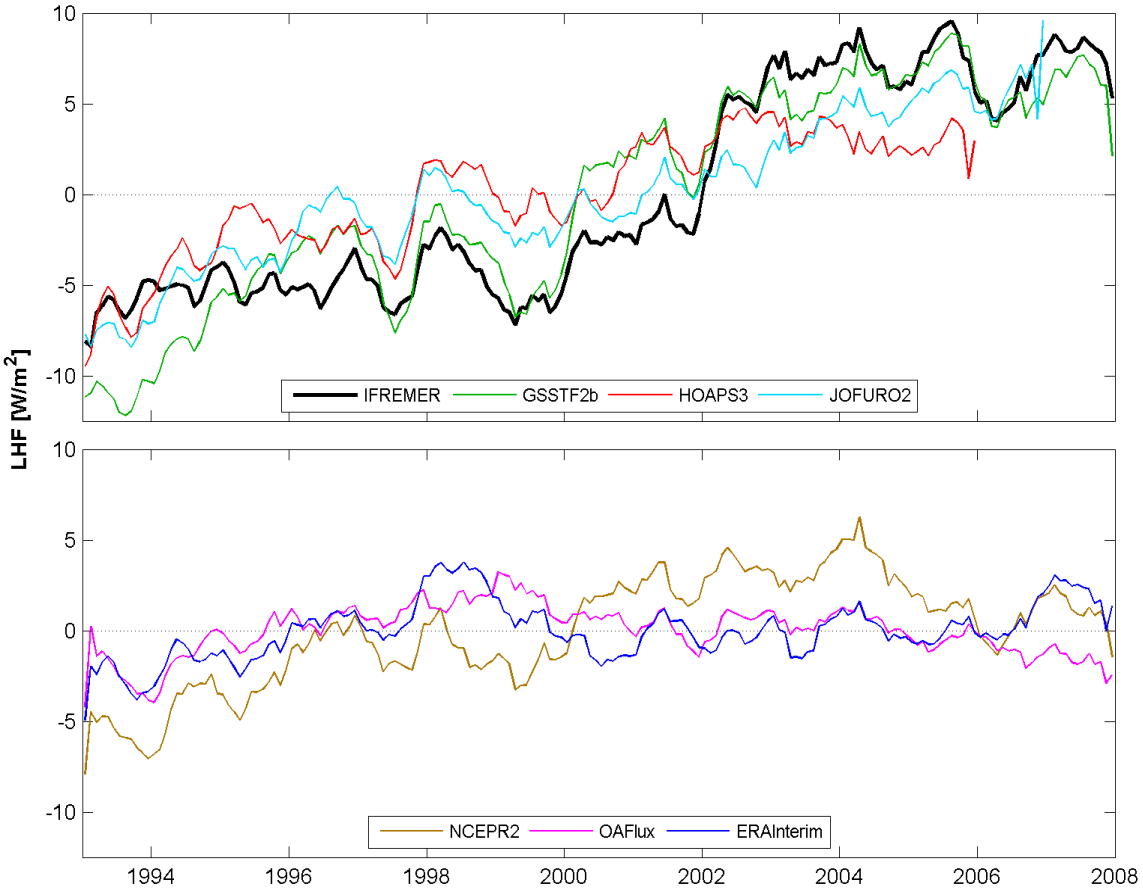

Figure 4. Anomaly time series of monthly LHF (in W/m2) over the ice-free ocean regions (45°S - 45°N). Each time series has been filtered using a 5-month, centered moving average.

5.2.2. Meteorological quantities: satellites

Figure 5 shows the anomaly time series of U_a, q_a, SST, and Δq for the four satellite products. The temporal extents match those in Figure 4. The time series of wind speed (Figure 5, top left) highlights an extensive amount of interannual variability. All of the datasets seem to track each other fairly closely except in the middle portion of time period. During this portion, significant differences between the datasets are apparent. From 1998 to 2002, U_a is biased high in HOAPS3 and low in IFREMER. Right around

2002, all datasets experience a large jump in U_a with IFREMER yielding the largest jump (~0.2 m/s greater than the other datasets). IFREMER's low bias prior to 2002 contributed to the exaggerated jump in wind speed. Furthermore, the exaggerated jump in wind speed likely contributed to the jump observed in the LHF. This issue is addressed in more detail in the discussion.

The time series of SST (Figure 5, bottom left) shows better correlation among datasets than U_a, and the 1997-1998 ENSO is evident within the observations. The better agreement occurs because the source of SST within each product takes advantage of similar satellite data, i.e., the AVHRR. IFREMER is biased slightly lower during the ENSO event, while HOAPS3 is biased higher during 2001-2002. Furthermore, IFREMER is biased slightly higher from approximately mid-2002 onward. While the reasons for some of these biases are not readily apparent, the bias in IFREMER after mid-2002 could be due to the use of AMSR in the SST dataset. This is another issue that is addressed the discussion.

Some of the biggest differences between the satellite products are seen in the time series of q_a (Figure 5, top right). The evolution of each time series is mostly similar, but the biases between datasets vary considerably. GSSTF2b is biased high relative to the other datasets for the first half, and it is biased low relative to the other datasets for the second half. HOAPS3 experiences an opposite effect in bias compared to GSSTF2b. IFREMER and J-OFURO2 track more closely to each other, and they mostly lie between the other two datasets.

The bottom-right panel in Figure 5 shows the time series of the humidity difference for the four satellite products. Based on the shape of these time series, one can conclude that the trends in LHF (Figure 4) are largely the result of trends in Δq. Similar to q_a, the biases of Δq vary considerably between products; this is to be expected since q_a is part of the equation for Δq. Figure 5 (bottom right) shows that GSSTF2b and IFREMER appear to have the largest trends in Δq, while HOAPS3 appears to have the smallest.

The values of the satellite bulk inputs given in Table 4 corroborate the qualitative trend differences seen in Figure 5. U_a and Δq contain significantly positive trends for all satellite-based datasets. Trends in U_a are virtually identical across all four products (~0.015 m/s/decade); accordingly, any differences in the LHF trend as a result of wind speed likely result from the discussed biases in U_a as opposed to U_a trends. Trends in Δq range from 0.036 g/kg/decade for the GSSTF2b to 0.02 g/kg/decade for the HOAPS3. The magnitudes of the observed Δq trends in Table 4 directly correlate to the magnitudes of the LHF trends. Trends in q_a are mostly negative across all products except HOAPS3, and only the GSSTF2b and IFREMER are significant. Therefore, q_a explains the significant Δq trends seen in GSSTF2b and IFREMER, while SST explains the significant Δq trends seen in HOAPS and J-OFURO2. Overall, the satellite-based products show large trends in LHF because of large trends in Δq.

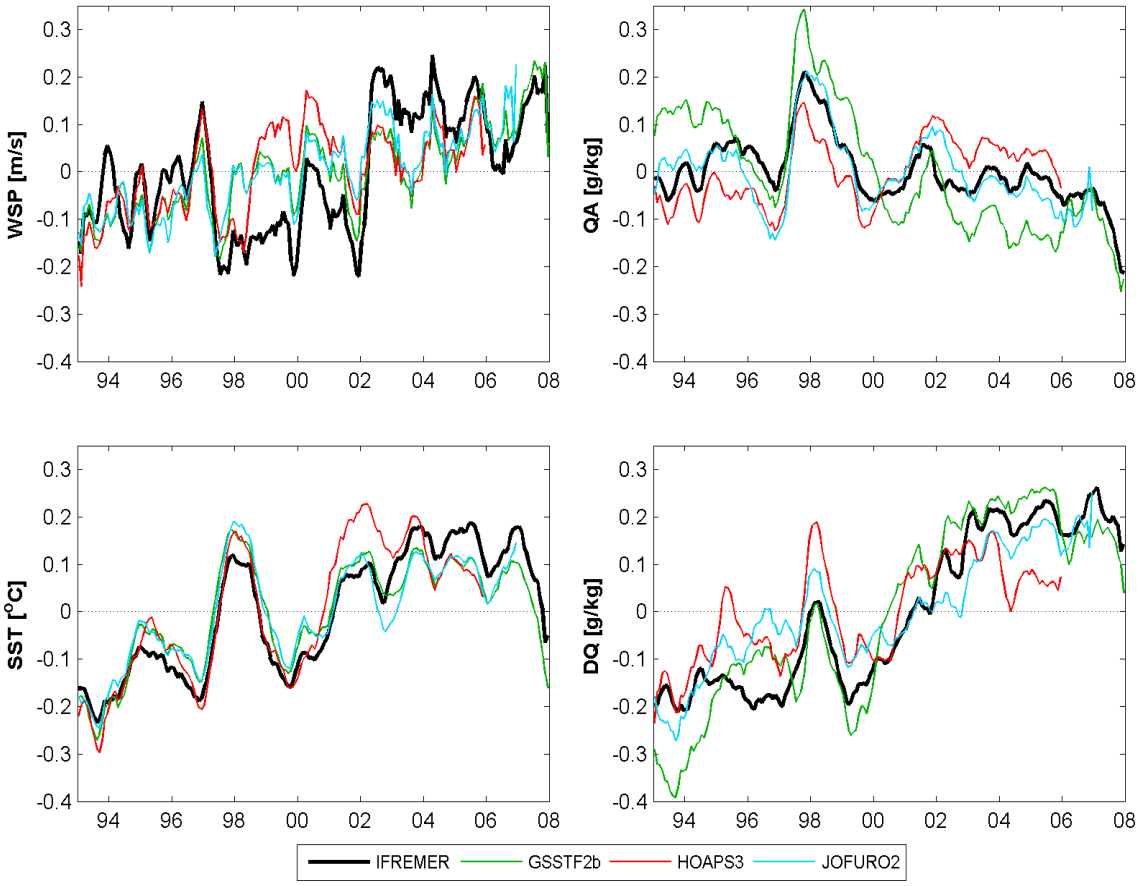

Figure 5. Anomaly time series of (top left) wind speed, (top right) specific humidity, (bottom left) sea surface temperature, and (bottom right) humidity difference ice-free ocean regions (45°S - 45°N) for the four satellite products. Units for each time series are listed to the left of the plot. All time series have been filtered using a 5-month, centered moving average.

Table 4. Global trends of LHF, Ua, qa, and Δq over the ice-free oceans (45°S - 45°N). All trends calculated from a 15-yr period except HOAPS (13-yr) and J-OFURO2 (14-yr). Trends that are significant at the 95% level are in boldface.

Trend (per decade)	Satellite				Reanalysis/Hybrid		
	GSSTF2b	HOAPS3	IFREMER	J-OFURO2	ERA Interim	NCEP-R2	OAFlux
LHF, W/m²	**1.226**	**0.768**	**1.148**	**0.933**	0.106	**0.486**	0.105
U_a, *m/s*	**0.016**	**0.015**	**0.014**	**0.016**	**0.006**	**0.011**	**0.012**
q_a, *g/kg*	**-0.023**	0.008	**-0.007**	-0.005	0.005	**0.013**	**0.019**
Δq, g/kg	**0.036**	**0.020**	**0.034**	**0.027**	**0.013**	0.003	-0.002

5.2.3. Meteorological quantities: reanalysis/hybrid

When looking at the state variables in Figure 6 for the two reanalyses and WHOI's OAFlux, more agreement exists relative to the satellite products. The time series of wind speed (Figure 6, top left) reveals that NCEP-R2 experiences a greater range in wind speed over the 15-yr period than the other two datasets. ERA-Interim and OAFlux track each other closely except during 2000 and 2006 where they diverge somewhat. All three products contain a positive trend in wind speed. The time series of SST (Figure 6, bottom left) shows close agreement between the three datasets; however, NCEP-R2 and OAFlux are in closest agreement. ERA-Interim is biased low between 2002 and 2005. Still, the SST's of the reanalysis/hybrid products are very similar to the satellite products (Figure 5, bottom left).

Looking at the time series of q_a in Figure 6 (top right), fewer discrepancies exist among the products relative to the satellite products in Figure 5 (top right). The greatest differences between all three products occur before 1997 and after 2002. OAFlux is slightly low-biased between 1993 and 1997, and high-biased from 2002 onward. ERA-Interim is slightly low-biased after 2005. All q_a datasets show a positive trend for the time period. The bottom-right panel in Figure 6 (bottom right) shows the various time series of humidity difference for the reanalysis/hybrid products. Clearly, the Δq trends are much flatter than the Δq trends of the satellite-based datasets (Figure 5, bottom right). In addition, fewer discrepancies in the Δq occur between reanalysis and hybrid products.

In Table 4, U_a is significantly positive for all three reanalysis/hybrid products, and except for ERA-Interim, the magnitude of the U_a trend is on par with the U_a trends seen

in the satellite products. ERA-Interim contains the only significantly positive trend in Δq. WHOI's Δq trend (-0.002 g/kg/decade) and NCEP-R2's Δq trend (0.003 g/kg/decade) are virtually non-existent. Conversely, WHOI and NCEP-R2 show significant positive trends in q_a. Of the three reanalysis/hybrid products, only NCEP-R2 shows any significant trend in LHF, which likely results from significant, positive trends in wind speed and near-surface specific humidity.

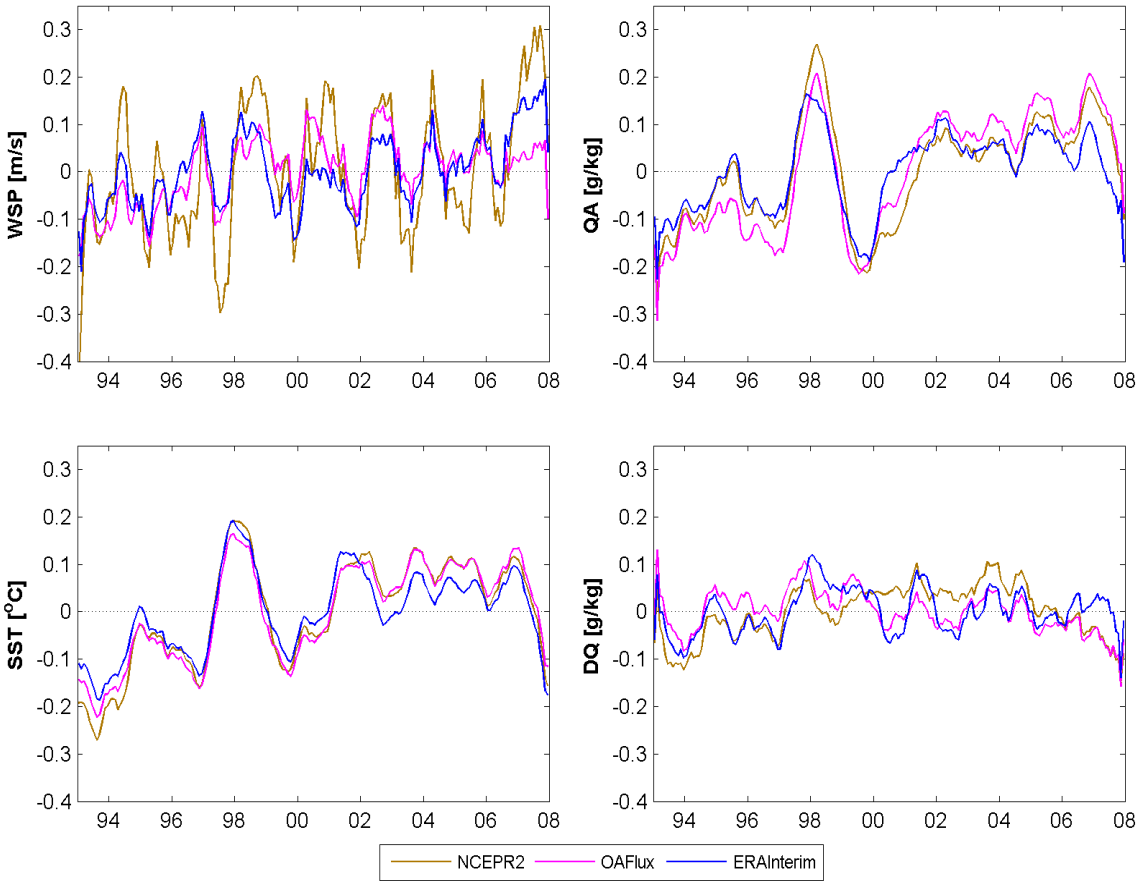

Figure 6. As in Figure 5, except for the three reanalysis/hybrid products.

5.3. Spatial Distribution of Trends

This study already analyzed globally-averaged trends. As an extension, the spatial patterns of the trends are examined as well. The distribution of the trends elucidates the origin of the global average values. Figures 7, 8, and 9 show the spatial distribution of trends in LHF, U_a, and Δq, respectively.

5.3.1. LHF

In Figure 7, spatial patterns of the LHF trends show some general, qualitative agreement across all seven products, but the magnitudes are vastly different. Some of the similarities between the products include negative trends in the Pacific cold tongue, large positive trends over the Pacific trade-wind belts, positive trends along the Northern and Southern Hemisphere boundary currents, and positive trends in the equatorial and sub-tropical Indian ocean. OAFlux has the most negative LHF trend in the cold tongue region, while NCEP-R2 has the largest positive LHF trend over the trade-wind belts. All products present a maximum, positive LHF trend in the Gulf Stream. For the remainder of the boundary currents, each product varies in the magnitude of the positive trend. In the Indian Ocean, magnitudes of LHF trend are greater in the satellite products than the reanalysis/hybrid products.

Differences among the seven products are readily apparent. The satellite products have positive trends over most of the global oceans; conversely, the reanalysis/hybrid products include large regions with negative LHF trends. Spatially, GSSTF2b and IFREMER exhibit the largest positive trends, while ERA-Interim and OAFlux exhibit the smallest negative trends. J-OFURO2 and HOAPS3 have positive trends over the global

oceans, but to a lesser degree than GSSTF2b and IFREMER. NCEP-R2 shows similarities with ERA-Interim and OAFlux, but it also contains extensive regions with very large positive trends that aren't present in the other two reanalysis/hybrid products. The pattern of the LHF trend in GSSTF2b and IFREMER explains why those products had the highest globally-averaged LHF trend. By the same token, the trend pattern observed in ERA-Interim and OAFlux explains why those products had the smallest globally-averaged latent heat flux trend.

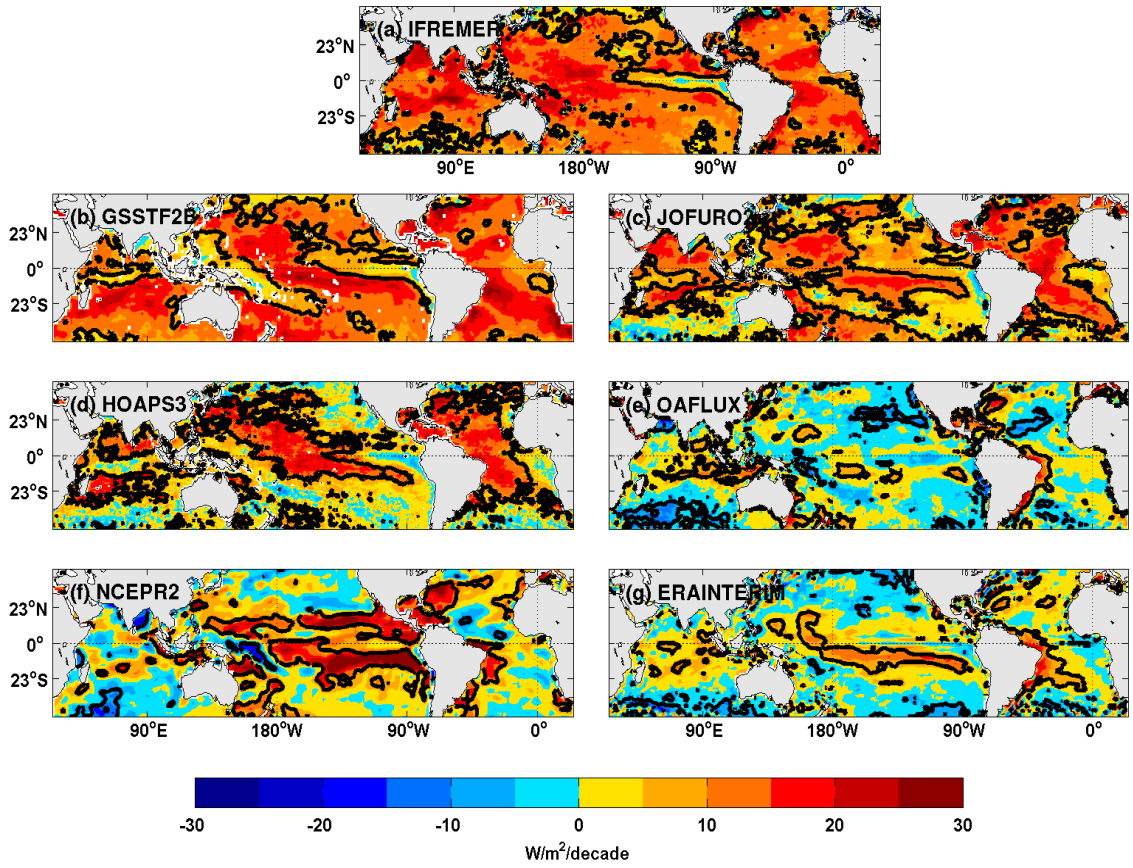

Figure 7. Spatial distributions of LHF trends (in W/m2 per decade) for (a) IFREMER, (b) GSSTF2b, (c) J-OFURO2, (d) HOAPS3, (e) OAFlux, (f) NCEP-R2, and (g) ERA-Interim. Trends are calculated on monthly data for January 1993 to December 2007, except for (c) and (d) whose period ends on December 2006 and December 2005, respectively. Thick solid contours enclose regions with trends that are significant at the 95% confidence level.

5.3.2. Wind speed

In Figure 8, the spatial distributions of the wind speed trends show a lot of agreement. The time series of global wind speed already showed similar magnitudes, so it is not unusual to find agreement in the spatial patterns as well. All products highlight a large region of positive trends in the equatorial/sub-tropical, eastern Pacific Ocean. The

region extends all the way to the central-western Pacific. The other common feature is two regions of positive trend in the Northern and Southern Atlantic with the Southern Atlantic showing more significance.

Some differences arise in the magnitudes of the wind speed trend. NCEP-R2 contains both the largest positive trends and the smallest negative trends. The large positive trends are contained the Pacific Ocean pattern previously described; the small negative trends occur in the higher latitude regions of the Pacific and the Atlantic. These regions of positive/negative trends in wind speed are common to all products but with a slighter magnitude. IFREMER does not contain many high latitude regions with a negative wind speed trend.

A loose correlation exists between the spatial pattern of U_a trends and the spatial pattern of LHF trends. The correlation between U_a and LHF trends is strongest in the Atlantic. NCEP-R2 seems to contain a stronger correlation between U_a and LHF trends in the Pacific than any other product. Overall, the spatial distribution of wind speed explains trends of LHF in the Atlantic better than in the Pacific.

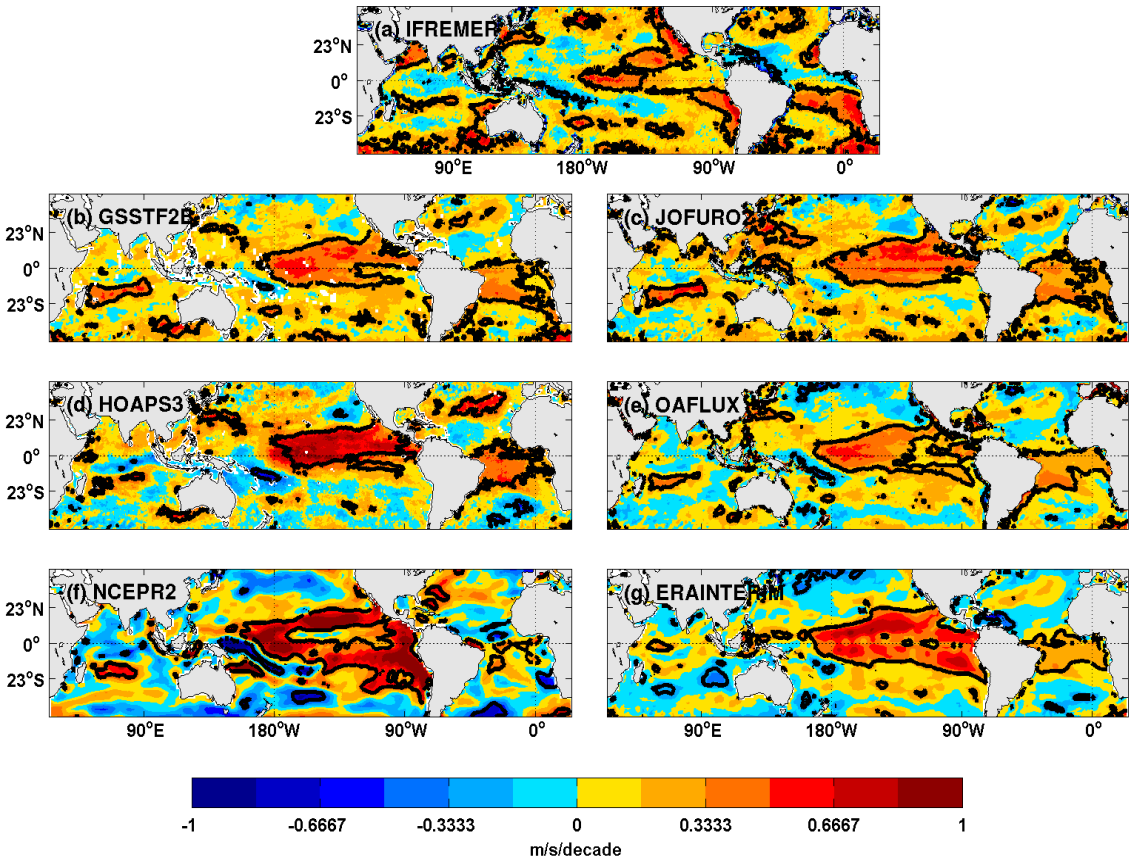

Figure 8. As in Figure 7, except for wind speed, Ua (in m/s per decade).

5.3.3. Humidity difference

Figure 9 shows maps of the trend in humidity difference. Similar to the interannual variability maps of LHF and Δq, the trend maps of LHF and Δq contain strikingly similar patterns. The same aspects of Figure 7 apply to Figure 9. Thus, the spatial trend in Δq explains most of the spatial trend in LHF.

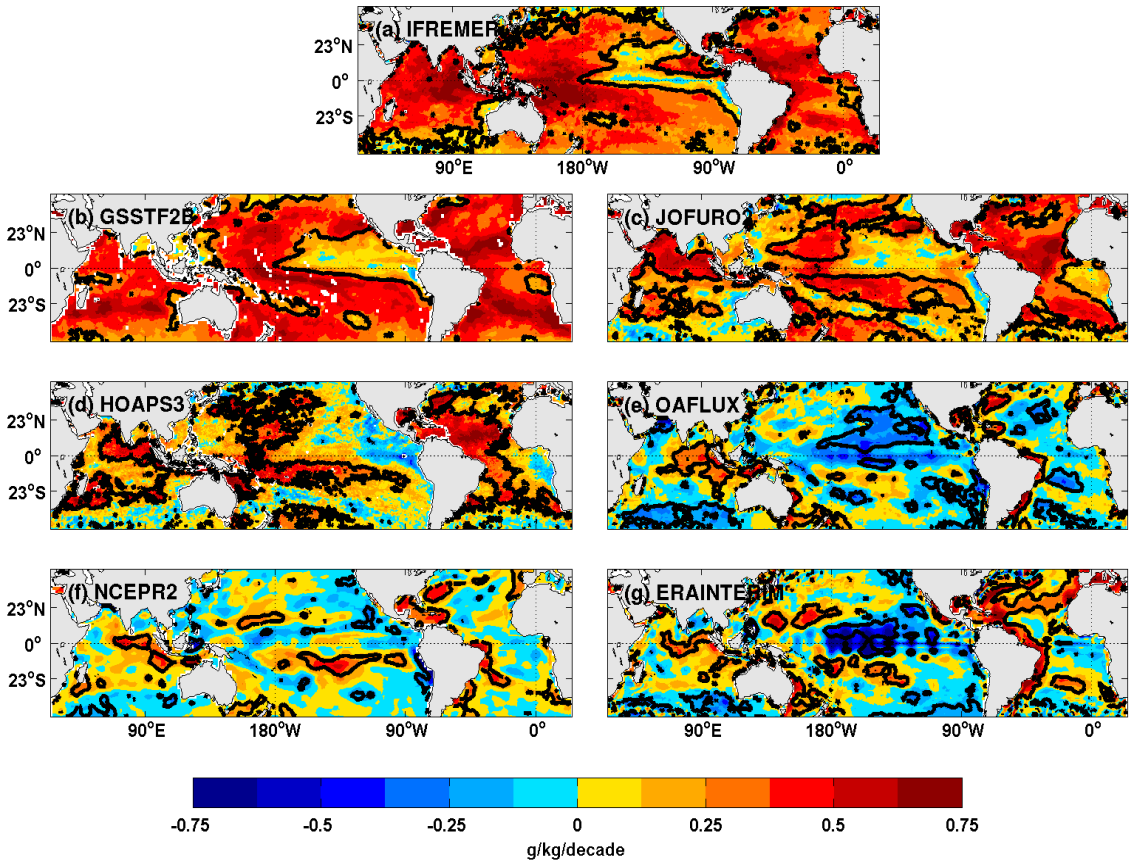

Figure 9. As in Figure 7, except for humidity difference, Δq (in g/kg per decade).

6. DISCUSSION

This study has shown that the IFREMER, satellite-derived, flux dataset exhibits good agreement with three other satellite datasets (GSSTF2b; HOAPS3; J-OFURO2); however, the satellite flux products exhibit both similarities and differences when compared with reanalyses (ERA-Interim; NCEP-R2) and WHOI's OAFlux. Examination of the interannual variability of latent heat flux reveals a common structure among all seven products. Regions of maximum LHF variability occur in the equatorial Pacific

Ocean, which is related to ENSO, and the western boundary currents, which are dominated by cold air outbreaks (Figure 1). Satellite products tend to show more LHF variability over the open oceans than the reanalysis/hybrid products, which leads to increased global means of LHF standard deviation. The NCEP-R2 exhibits the highest global mean of LHF standard deviation of any product (Table 3). Differences in the magnitude of LHF variability result from differences in the magnitude of variability for the bulk variables, i.e., q_a, U_a, Δq, and SST. The global LHF pattern appears to be largely controlled by variations in Δq, but variations in U_a have some influence, particularly within the tropical Pacific. Moreover, LHF variability is indirectly related to SST variability because SST modulates both Δq and q_a.

The effects of SST and U_a on LHF are most obvious in the tropical Pacific where ENSO is the regulating mechanism. During warm ENSO episodes, tropical Pacific water from the western warm pool migrates eastward, replacing normally cooler water. The change in spatial distribution of warm water alters the humidity gradient between the surface and the atmosphere. In addition, easterly trade winds relax or even reverse direction, further increasing the buildup of warmer water in the eastern tropical Pacific and modifying the magnitude of evaporation. ENSO is a quasi-periodic, ocean-atmosphere mode that occurs every five years on average, which influence interannual (3–8 yr) timescales. The effect of ENSO on SST, which relates to Δq and U_a, explains the standard deviation pattern of LHF observed in the Pacific.

Interannual variability of LHF over the western boundary currents is modulated by synoptic, winter storms, also known as cold air outbreaks. During the winter, mid-

latitude cyclones leaving a continental land mass encounter warm waters within the boundary currents. The air within the cyclone is dry, while the air just above the ocean surface is moist. Hence, an intense humidity gradient is formed as the cyclone enters the region above the boundary current. Large amounts of heat and moisture transfer from the water's surface to the atmosphere during these events. Temporal variability of these wintertime outbreaks has a controlling influence on the interannual variability of LHF over boundary currents.

Examination of trends in latent heat flux and the associated bulk variables revealed more differences between the two sets of products than was observed in the interannual variability. All four satellite products exhibit large yet significant, positive trends in LHF; reanalysis/hybrid products exhibit much smaller, positive trends in LHF (Table 4). IFREMER and GSSTF2b have the largest global LHF trends because they show positive trends over the majority of the oceans. One reason for the observed LHF trends is the significant, positive trends in wind speed (Table 4). Yet, the trend in wind speed is similar for all four satellite products, so it doesn't account for the larger trends seen in IFREMER and GSSTF2b. Trends in humidity difference may also be partly responsible. The magnitudes of the global trends in Δq directly correlate with the magnitudes of the global trends in LHF for all satellite products (Table 4). Likewise, the spatial patterns in the trend of Δq and LHF correspond better than the spatial patterns in the trend of U_a and LHF. This correspondence is true for all products.

The reasons for the larger Δq trends in satellites may be related to SST, q_a, or both. All seven products show a positive trend in SST over the 15-yr period, but some of

the satellite products, especially the IFREMER, show a slightly bigger trend in SST (Figure 5). Thus, SST represents one reason why Δq is larger in the satellite-derived datasets. When examining q_a, three of the four satellites exhibit a negative trend, while all of the reanalysis/hybrid products exhibit a positive trend. A negative overall trend in q_a imposes a more positive trend in Δq. Hence, q_a is a second reason why the satellite products show an increased trend in Δq. Finally, when the two variables are combined to calculate Δq, the opposite trends bring about an even more positive trend in Δq. It is impossible to say which product gives the "most" accurate calculation of the humidity difference. Nevertheless, this analysis is able to provide an uncertainty range of the trend in Δq (-0.002 to 0.036 g/kg/decade) and a corresponding uncertainty range of the trend in LHF (0.11 to 1.23 W/m^2/decade).

Further exploration of the bulk variables, including source of the observations and method of calculation, can reveal more insight into the difference in LHF trends from the IFREMER and other satellite products. *Shie* [2010] points out one reason for the LHF trend seen in the GSSTF2b. He notes a slightly decreasing trend in SSM/I T_B, which is used to retrieve W_B. Since W_B is used in the calculation of specific air humidity, it leads to a larger trend in the humidity difference. *Santorelli et al.* [2011] also found that specific air humidity contributes to the larger biases found in IFREMER. Their solution was to utilize a different method for calculating humidity from *Jackson et al.* [2006, 2009]. Based on comparisons with buoy measurements, *Santorelli et al.* [2011] showed that the new humidity algorithm improves the LHF estimates in IFREMER. Furthermore, they alluded to a discrepancy in SST around 2002 resulting from use of the

merged, Reynolds SST analysis. The merged SST analysis takes advantage of the AMSR satellite instrument starting in June 2002. Their conclusion was that the discontinuity observed in 2002 is an artifact of the merging process between the AVHRR and the AMSR instruments.

As mentioned, the global IFREMER trend of LHF was one of the highest. It was shown in the results that the trend is overwhelmed by a rapid increase in LHF centered around 2002 (Figure 4). The SST discontinuity noted by *Santorelli et al.* [2011] is also observed in this study (Figure 5, bottom left). Furthermore, this study pointed out a large jump in wind speed around 2002 for the IFREMER dataset (Figure 5, top left). One of these issues alone likely does not account for the rapid increase in LHF, but when combined with the calculation of air humidity, all issues could account for the rise seen in latent heat flux.

Figure 10 examines the effect of SST on LHF with and without the ASMR instrument. The effect is only analyzed for June 2002 to December 2007, or the time period that the AMSR was in operation for this study. In the left panel of Figure 10, it is shown that inclusion of the AMSR produces a bias of 0.055°C. The resulting SST bias produces a LHF bias of 2.1 W/m^2. A LHF bias of this magnitude is not excessive, but its effect is enough to slightly elevate all flux estimates from June 2002 onward. The bias does not suggest that the merged SST analysis is wrong; it just shows that the SST analysis using only the AVHRR is temporally consistent for the 15-yr period considered in this study. Differences between the two SST products likely result from sampling

frequency. The merged SST analysis still performs better from 2002 onwards because of improved spatial resolution afforded by the AMSR [*Reynolds et al.*, 2007].

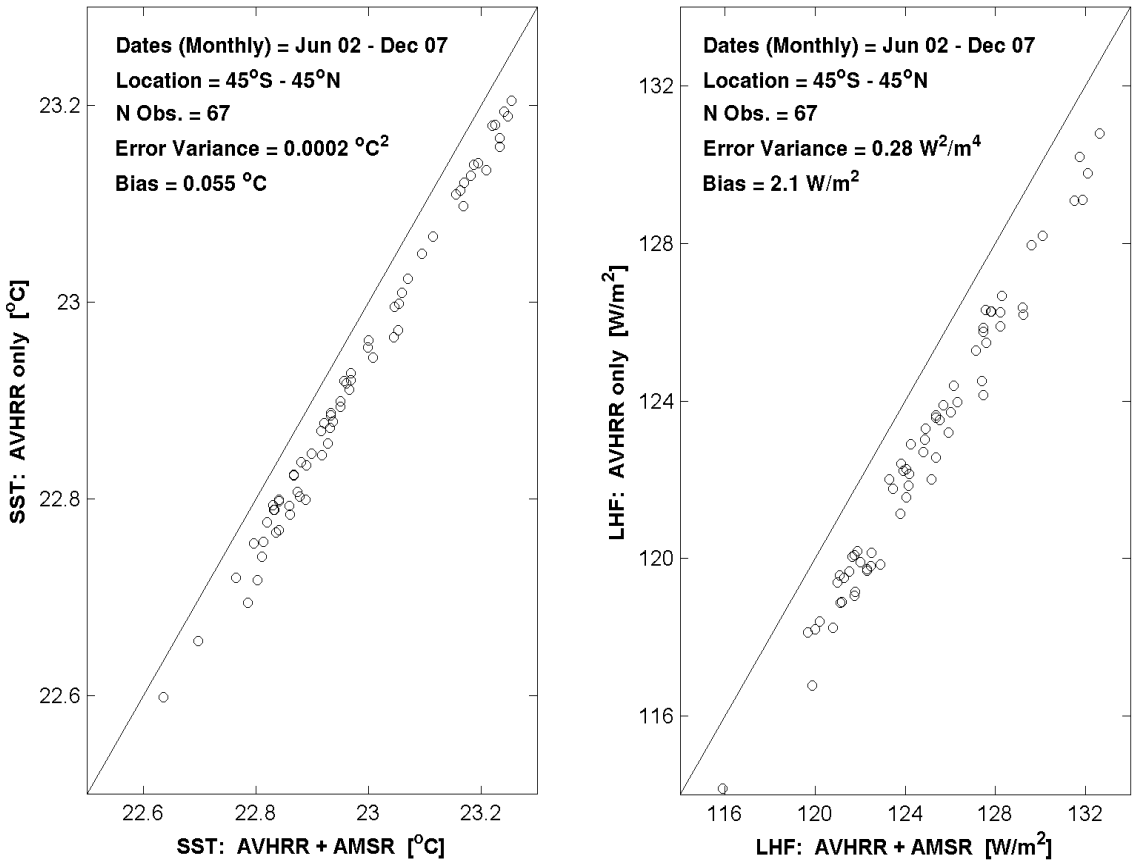

Figure 10. Comparisons of (left) SST and (right) LHF between the two different analyses of Reynolds (2007): the analysis using only AVHRR and the analysis using AVHRR+AMSR. Comparisons only cover the period of AMSR availability. LHF is calculated using the COARE 3.0 algorithm and state variables from IFREMER except for SST, which is taken from each of the Reynolds' analyses.

Figures 11 and 12 dissect the anomalous wind speed jump seen in IFREMER. The wind speed product of IFREMER merges wind estimates from scatterometers and SSM/I's. An optimum interpolation process known as kriging determines the magnitude

of spatio-temporal contributions from SSM/I's and scatterometers [*Bentamy et al.*, 1999]. Figure 11 shows the merged, IFREMER winds along with QuickSCAT winds and SSM/I-F13 winds. During the period when the wind speed jump is observed, QuickSCAT was the only scatterometer incorporated into the merged product. The F13 was not the only SSM/I instrument incorporated into the merged product around 2002, but only F13 is presented here because it should represent the temporal evolution of all SSM/I's. From October 2001 to June 2002, Figure 11 shows that IFREMER experiences a ~0.6 m/s increase in wind speed, while QuickSCAT and F13 experience smaller increases in wind speed. More importantly, QuickSCAT is biased higher than F13 during this period. Thus, the merging process likely combines the biases of the two instruments during this period, forming a merged product that contains an exaggerated jump in wind speed around 2002.

Figure 12 further examines IFREMER wind speed by looking at the slope of wind speed over the same 2001-2002 period. The top panel in Figure 12 shows regions with the greatest slope in wind speed occur at the southern high latitudes. The remaining two panels in Figure 12 give the differences in wind speed slopes between IFREMER and respectively, the F13 and the QuickSCAT. Figure 12 (middle panel) shows that the F13 contains a larger slope than IFREMER over most oceans. Conversely, QuickSCAT contains a smaller slope than IFREMER over most oceans except in the high-latitude north Pacific and north Atlantic (Figure 12, bottom panel). Therefore, the wind speed jump seen in IFREMER during 2001 and 2002 likely results from a larger increase in SSM/I wind speed.

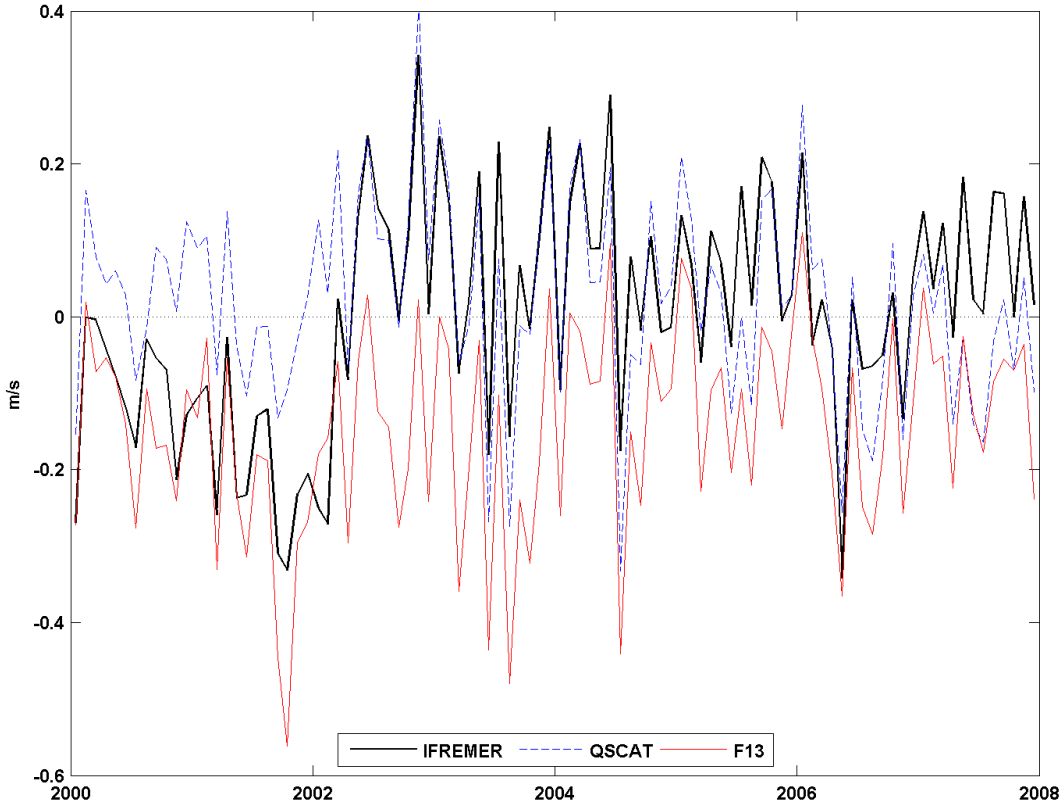

Figure 11. Global anomaly time series of wind speed from IFREMER, QuickSCAT, and SSM/I aboard the F13 satellite. Global averages are taken over ice-free oceans (45°S - 45°N). Temporal periods of IFREMER and F13 are truncated to match the shorter period of the QuickSCAT.

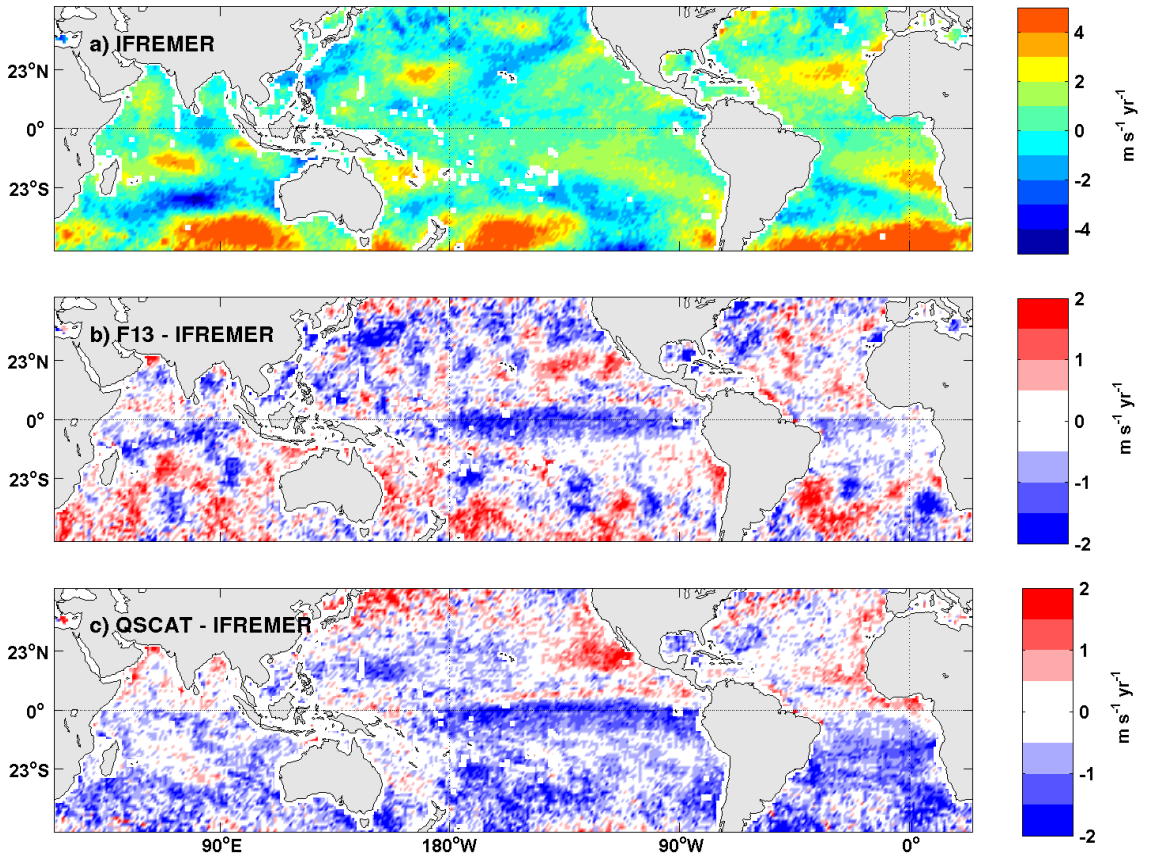

Figure 12. (a) Slope of wind speed from IFREMER for period Oct 2001 to June 2002. Difference in slopes of IFREMER versus (b) F13 and (c) QuickScat over the same time period.

Since the effect of specific air humidity on IFREMER's LHF has been investigated thoroughly by *Santorelli et al.* [2011], this study only briefly looks at the effect of trends in LHF as a result of q_a. Figure 13 shows global time series of LHF using three different sources of q_a. The LHF calculation is performed using the COARE 3.0 bulk algorithm, and the remaining bulk variables come from IFREMER. Thus, Figure 13 illustrates the effect of q_a on the LHF trend in IFREMER. Notably, the LHF trends decrease significantly using other estimates of specific air humidity largely because of

smaller anomalies at the beginning of the time series. A jump in LHF still occurs around 2002, but to a lesser degree than with q_a estimated by IFREMER.

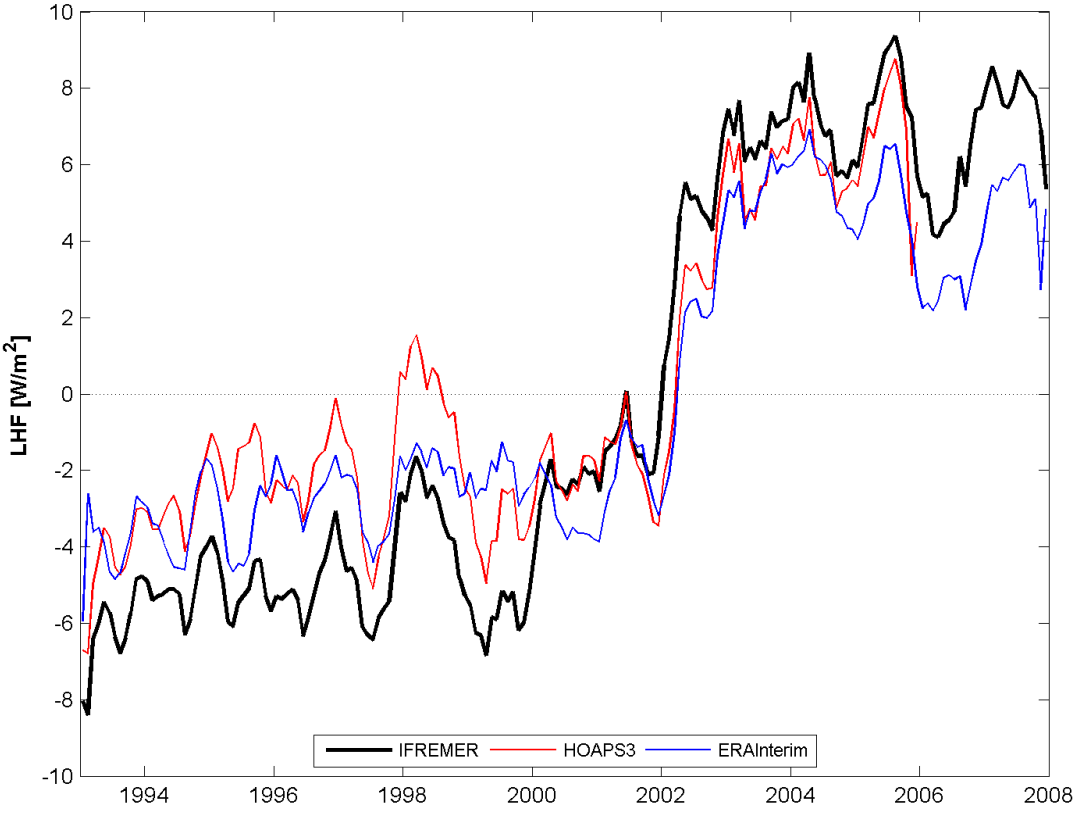

Figure 13. Global anomaly time series of LHF using qa from three different sources. LHF is recalculated using COARE 3.0 with state variables from IFREMER and the listed qa source.

Going forward, the IFREMER turbulent flux dataset should be reexamined to address some of the issues raised in this study. IFREMER and other satellite-derived flux products already deliver an effective climatology of LHF over the global oceans [*Schlosser and Houser*, 2007], and they provide better flux estimates for forcing ocean models [*Ayina et al.*, 2006]. Still, satellite products need to be studied further to determine their effectiveness in longer term climate studies. Satellites provide an

advantage over reanalyses because they observe and sample the Southern Hemisphere ocean. As bulk flux algorithms are improved, satellite-derived datasets should become the baseline for estimates of latent heat flux.

References

Andersson, A., Fennig, K., Klepp, C., Bakan, S., Graßl, H., and Schulz, J. (2010), The Hamburg Ocean Atmosphere Parameters and Fluxes from Satellite Data - HOAPS-3, *Earth Syst. Sci. Data Discuss.*, *3*, 143–194.

Ashok, K., S. K. Behera, S. A. Rao, H. Weng, and T. Yamagata (2007), El Niño Modoki and its possible teleconnection, *J. Geophys. Res.*, *112*.

Ayina, L.-H., A. Bentamy, A. M. Mestas-Nuñez, and G. Madec (2006), The impact of satellite winds and latent heat fluxes in a numerical simulation of the tropical Pacific Ocean, *J. Climate*., *19*, 5889–5902.

Baumgartner, A., and E. Reichel (1975), *The World Water Balance: Mean Annual Global, Continental and Maritime Precipitation, Evaporation, and Run-off,* Elsevier, 179 pp.

Beljaars, A. C. M. (1995), The parameterization of surface fluxes in large scale models under free convection, *Quart. J. Roy. Meteor. Soc.*, *121*, 255–270.

Bentamy, A., P. Queffeulou, Y. Quilfen, and K. Katsaros (1999), Ocean surface wind fields estimated from satellite active and passive microwave instruments. *IEEE Trans. Geosci. Remote Sens., 37***,** 2469–2486.

Bentamy, A., K. B. Katsaros, A. M. Mestas-Nuñez, W. M. Drennan, E. B. Forde, and H. Roquet (2003), Satellite estimates of wind speed and latent heat flux over the global oceans, *J. Climate*, *16*, 637–656.

Blanke, B., and P. Delecluse (1993), Variability of the tropical Atlantic Ocean simulated by a general circulation model with two different mixed layer physics, *J. Phys. Oceanogr., 23***,** 1363–1388.

Bouras, D., L. Eymard, and W. T. Liu (2002), A neural network to estimate the latent heat flux over oceans from satellite observations, *Int. J. Remote Sens., 23***,** 2405–2423.

Bouras, D. (2006), Comparison of Five Satellite-Derived Latent Heat Flux Products to Moored Buoy Data, *J. Climate*, *19*, 6291–6313.

Brunke, M. A., C. W. Fairall, X. Zeng, L. Eymard, and J. A. Curry (2003), Which bulk aerodynamic algorithms are least problematic in computing ocean surface turbulent fluxes?, *J. Climate, 16***,** 619–635.

Casey, K. S. (2004), Global AVHRR 4 km SST for 1985–2001, Pathfinder V5.0, ODC/RSMAS, Technical report, NOAA National Oceanographic Data Center, Silver Spring, Maryland. NODC Accession Numbers 0001763-0001864: Pathfinder AVHRR Version 5.0.

Casey, K. S., and P. Cornillon (2001), Global and regional sea surface temperature trends, *J. Climate, 14***,** 3801–3818.

Chou, S.-H. (1993), A comparison of airborne eddy correlation and bulk aerodynamic methods for ocean–air turbulent fluxes during cold-air outbreaks, *Bound.-Layer Meteor., 64***,** 75–100.

Chou, S.-H., R. M. Atlas, C.-L. Shie, and J. Ardizzone (1995), Estimates of surface humidity and latent heat fluxes over oceans from SSM/I data, *Mon. Wea. Rev., 123***,** 2405–2425.

Chou, S.-H., C.-L. Shie, R. M. Atlas, and J. Ardizzone (1997), Air–sea fluxes retrieved from Special Sensor Microwave Imager data, *J. Geophys. Res., 102***,** 12 705–12 726.

Chou, S.-H., E. Nelkin, J. Ardizzone, R. M. Atlas, and C.-L. Shie (2003), Surface turbulent heat and momentum fluxes over global oceans based on the Goddard satellite retrievals, version 2 (GSSTF2), *J. Climate, 16***,** 3256–3273.

Chou, S. H., E. Nelkin, J. Ardizzone, R. M. Atlas, and C. L. Shie (2004) A comparison of latent heat fluxes over global oceans for four flux products, *J. Climate, 17***,** 3973–3989.

Curry, J., and Coauthors (2004), SEAFLUX, *Bull. Amer. Meteor. Soc., 85***,** 409–424.

da Silva, A., C. C. Young, and S. Levitus (1994), *Atlas of Surface Marine Data 1994.* Vol. 1: *Algorithms and Procedures, NOAA Atlas NESDIS 6,* U.S. Department of Commerce, Washington, DC, 83 pp.

Dee, D. P. and Coauthors (2011), The ERA-Interim reanalysis: Configuration and performance of the data assimilation system, *Q. J. R. Meteorol. Soc.*, *137(656)*, 553–597.

Deser, C., A. S. Phillips, and M. A. Alexander (2010), Twentieth century tropical sea surface temperature trends revisited, *Geophys. Res. Lett.*, *37*.

Dyer, A. J. (1974), A review of flux-profile relationships, *Bound.-Layer Meteor.*, *7*, 363–372.

Fairall, C. W., E. F. Bradley, D. P. Rogers, J. B. Edson, and G. S. Young (1996a), Bulk parameterization of air–sea fluxes in TOGA COARE, *J. Geophys. Res., 101***,** 3747–3767.

Fairall, C. W., E. F. Bradley, J. S. Godfrey, G. A. Wick, J. B. Edson, and G. S. Young, (1996b), Cool skin and warm layer effects on the sea surface temperature, *J. Geophys. Res., 101*, 1295–1308.

Fairall, C. W., E. F. Bradley, J. E. Hare, A. A. Grachev, and J. B. Edson (2003), Bulk parameterization of air–sea fluxes: Updates and verification for the COARE algorithm, *J. Climate, 16***,** 571–591.

Fennig, K., S. Bakan, H. Grassl, C.-P. Klepp, and J. Schulz (2006), Hamburg Ocean Atmosphere Parameters and Fluxes from Satellite Data – HOAPS II – Monthly Mean, World Data Cent. for Clim., Hamburg, Germany.

Grassl, H., V. Jost, R. Kumar, J. Schulz, P. Bauer, and P. Schluessel (2000), The Hamburg Ocean-Atmosphere Parameters and Fluxes from Satellite Data (HOAPS): A climatological atlas of satellite-derived air-sea-interaction parameters over the oceans, *Tech. Rep. 312*, Max Planck Institute for Meteorology, Hamburg, Germany, 130 pp.

Grima, N., A. Bentamy, P. Delecluse, K. Katsaros, C. Levy, and Y. Quilfen (1999), Sensitivity of an Oceanic general circulation model forced by satellite wind stress fields, *J. Geophys. Res., 104*, 7967–7989.

Grodsky, S. A., A. Bentamy, J. A. Carton, and R. T. Pinker (2009), Intraseasonal latent heat flux based on satellite observations, *J. Climate*, *22*, 4539–4556.

Holtslag, A. A. M., and H. A. R. DeBruin (1988), Applied modeling of the nighttime surface energy balance over land, *J. Appl. Meteorol.*, *27*, 689–704.

Iwasaki, S., M. Kubota, and H. Tomita (2010), Evaluation of bulk method for satellite-derived latent heat flux, *J. Geophys. Res.*, *115*.

Jackson, D.L., G. A. Wick, and J. J. Bates (2006), Near-surface retrieval of air temperature and specific humidity using multisensory microwave satellite observations, *J. Geophys. Res*., *111.*

Jackson, D. L., G. A. Wick, and F. R. Robertson (2009), Improved multi-sensor approach to satellite-retrieved near-surface specific humidity observations. *J. Geophys. Res.*, *114*.

Jones, C., P. Peterson, and C. Gautier (1999), A new method for deriving ocean surface specific humidity and air temperature: An artificial neutral network approach, *J. Appl. Meteorol.*, *38*, 1229– 1245.

Kalnay, E., and Coauthors (1996), The NCEP/NCAR 40-Year Reanalysis Project, *Bull. Amer. Meteor. Soc., 77***,** 437–471.

Kanamitsu, M., W. Ebisuzaki, J. Woollen, S. K. Yang, J. J. Hnilo, M. Fiorino, and G. L. Potter (2002), NCEP–DOE AMIP-II reanalysis (R-2), *Bull. Amer. Meteor. Soc., 83***,** 1631–1643.

Kiehl, J. T., and K. E. Trenberth (1997), Earth's annual global mean energy budget, *Bull. Amer. Meteor. Soc., 78***,** 197–208.

Klein, S. A., B. J. Soden, and N.-C. Lau (1999), Remote sea surface variations during ENSO: Evidence for a tropical atmospheric bridge, *J. Climate, 12***,** 917–932.

Krasnopolsky, V. M., B. L. C., and W. H. Gemmill (1995), A neural network as a nonlinear transfer function model for retrieving surface wind speeds from the SSM/I, *J. Geophys. Res*., *100*, 11 033–11 045.

Kubota, M., N. Iwasaka, S. Kizu, M. Konda, and K. Kutsuwada (2002), Japanese Ocean Flux data sets with Use of Remote sensing Observations (J-OFURO), *J. Oceanogr., 58***,** 213–225.

Kubota, M., A. Kano, H. Muramatsu, and H. Tomita (2003), Intercomparison of various surface latent heat flux fields, *J. Climate, 16***,** 670–678.

Large, W. G., and S. Pond (1982), Sensible and latent heat flux measurements over the oceans, *J. Phys. Oceanogr., 12***,** 464–482.

Lau, N.-C, and M. J. Nath (1994), A modeling study of the relative roles of tropical and extratropical SST anomalies in the variability of the global atmosphere–ocean system, *J. Climate, 7***,** 1184–1207.

Liu, J. and J.A. Curry (2006), Variability of the tropical and subtropical ocean surface latent heat flux during 1989-2000, *Geophys. Res. Lett.*, *33*.

Liu, W. T. (1986), Statistical relation between monthly mean precipitable water and surface-level humidity over global oceans, *Mon. Wea. Rev., 114***,** 1591–1602.

Liu, W. T. (1988), Moisture and latent heat flux: Variabilities in the tropical Pacific derived from satellite data, *J. Geophys. Res., 93***,** 6749–6769.

Liu, W. T., K. B. Katsaros, and J. A. Businger (1979), Bulk parameterization of air–sea exchanges of heat and water vapor including the molecular constraints at the interface, *J. Atmos. Sci., 36***,** 1722–1735.

Mestas-Nuñez, A. M., A. Bentamy, and K. B. Katsaros (2006), Seasonal and El Niño variability in weekly satellite evaporation over the global ocean during 1996–98, *J. Climate, 19***,** 2025–2035.

Monin, A. S. and Obukhov, A. M. (1954), Basic laws of turbulent mixing in the ground layer of the atmosphere, *Akad. Nauk. SSSR Geofiz. Inst. Tr., 151*, 163–187.

Murray, F. W. (1967), On the computation of saturation vapor pressure, *J. Appl. Meteor.*, *6*, 203–204.

Reynolds, R.W., T.M. Smith, C. Liu, D.B. Chelton, K.S. Casey, and M.G. Schlax (2007), Daily High-Resolution-Blended Analyses for Sea Surface Temperature, *J. Climate*, *20*, 5473–5496.

Santorelli, A., R. T. Pinker, A. Bentamy, K. B. Katsaros, W. M. Drennan, A. M. Mestas-Nuñez, and J. A. Carton (2011), Differences between two estimates of air-sea turbulent heat fluxes over the Atlantic Ocean, *J. Geophys. Res.*, *116*.

Schlosser, C. A., and P. R. Houser (2007), Assessing a satellite-era perspective of the global water cycle, *J. Climate, 20***,** 1316–1338.

Schlüssel, P., L. Schanz, and G. English (1995), Retrieval of latent heat flux and long wave irradiance at the sea surface from SSM/I and AVHRR measurements, *Adv. Space Res., 16***,** 107–115.

Schulz, J., P. Schlüssel, and H. Graßl (1993), Water vapor in the atmospheric boundary layer over oceans from SSM/I measurements, *Int. J. Remote Sens., 14***,** 2773–2789.

Schulz, J., J. Meywerk, S. Ewald, and P. Schluessel (1997), Evaluation of satellite-derived latent heat fluxes, *J. Climate, 10***,** 2782–2795.

Shie, C.-L., L. S. Chiu, R. Adler, P. Xie, I-I Lin, F.-C. Wang, E. Nelkin, R. Chokngamwong, W. S. Olson, and D. A. Chu (2009), A note on reviving the Goddard Satellite-based Surface Turbulent Fluxes (GSSTF) dataset, *Adv. in Atmospheric Sciences*, 26(6), 1071-1080.

Shie, C.-L. (2010), Science background for the reprocessing and Goddard Satellite-based Surface Turbulent Fluxes (GSSTF2b) Data Set for Global Water and Energy Cycle Research. Science Document for the Distributed GSSTF2b via Goddard Earth Sciences (GES) Data and Information Services Center (DISC), 18 pp.

Smith, S. D. (1988), Coefficients for sea surface wind stress, heat flux and wind profiles as a function of wind speed and temperature, *J. Geophys. Res., 93***,** 15 467–15 472.

Smith, S. R., P. J. Hughes and M. A. Bourassa (2010), A comparison of nine monthly air-sea flux products, *Int. J. Climatol.*, *31*, 1002–1027.

Tiao, G. C., G. C. Reinsel, D. Xu, J. H. Pedrick, X. Zhu, A. J. Miller, J. J. DeLuisi, C. L. Mateer, and D. J. Wuebbles (1990), Effects of autocorrelation and temporal samplings schemes on estimates of trend and spatial correlation, *J. Geophys Res.*, *95*, 20 507–20 517.

Tomita, H.,M. Kubota, M. F. Cronin, S. Iwasaki, M. Konda, and H. Ichikawa (2010), An assessment of surface heat fluxes from J- OFURO2 at the KEO and JKEO sites, *J. Geophys. Res.*, *115*.

Trenberth, J. E., J. T. Fasullo, and J. Kiehl (2009), Earth's global energy budget, *Bull. Am. Meteorol. Soc.*, *90*, 311–323.

Uppala, S. M., and Coauthors (2005), The ERA40 reanalysis, *Quart. J. Roy. Meteor. Soc., 131*, 2961–3012.

Wentz, F. J. (1997), A well-calibrated ocean algorithm for SSM/I, *J. Geophys. Res., 102*, 8703–8718.

Wentz, F. J., and P. D. Ashcroft (1996), SSM/I and ECMWF Wind Vector Comparison.

Wentz, F. J., L. Ricciardulli, K. Hilburn, and C. Mears (2007), How much more rain will global warming bring?, *Science*, *317*, 233–235.

Worley, S. J., S. D. Woodruff, R. W. Reynolds, S. J. Lubker, and N. Lott (2005), ICOADS release 2.1 data and products, *Int. J. Climatol., 25*, 823–842.

Yu, L., X. Jin, and R. A. Weller (2006), Role of Net Surface Heat Flux in Seasonal Variations of Sea Surface Temperature in the Tropical Atlantic Ocean, *J. Climate*, *19*, 6153–6169.

Yu, L., and R.A. Weller (2007), Objectively analyzed air–sea heat fluxes for the global ice-free oceans (1981–2005), *Bull. Amer. Meteor. Soc.*, *88*, 527–539.

Yu L, Jin X, Weller RA (2008), Multidecade global flux datasets from the Objectively Analyzed Air-Sea Fluxes (OAFlux) Project: Latent and sensible heat fluxes, ocean evaporation, and related surface meteorological variables, *OAFlux Project*

Tech. Rep. OA-2008-01, Woods Hole Oceanographic Institution, Woods Hole, MA.

Zhang, C., and M. J. McPhaden (2000), Intraseasonal surface cooling in the equatorial western Pacific, *J. Climate, 13***,** 2261–2276.